Developmental Cell

Article

Length limitation of astral microtubules orients cell divisions in murine intestinal crypts

Graphical abstract

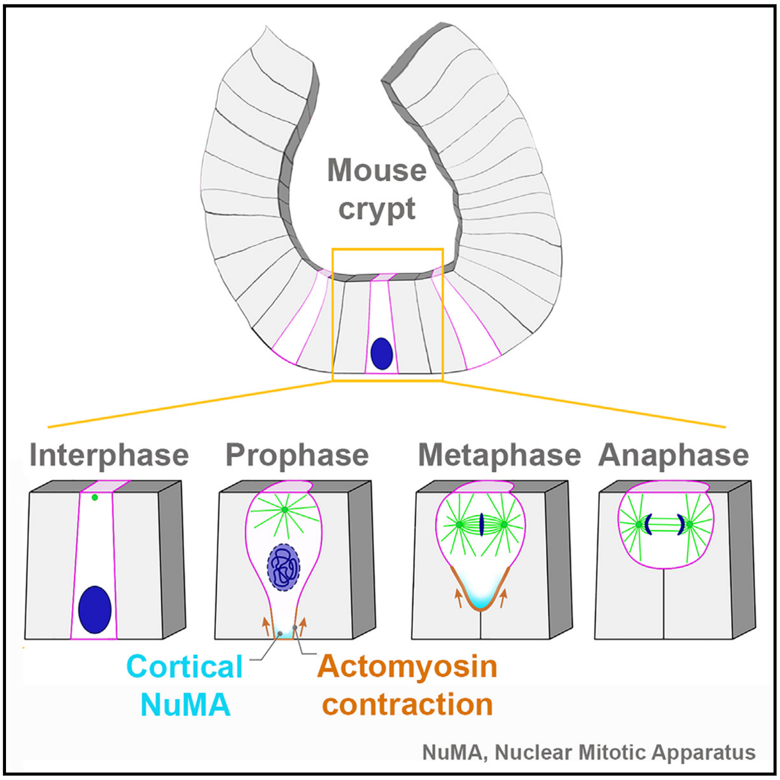

Highlights

- Planar spindle orientation is independent of polarity cues in intestinal organoids
- Astral microtubules are limited in length on the basal side of mitotic cells
- Length limitation allows spindles to probe apical cell shapes to orient planarly
- Planar spindle orientation safeguards epithelium architecture

Authors

Jad Saleh, Marc-Antoine Fardin, Amlan Barai, ..., Audrey Vincent, Nicolas Minc, Delphine Delacour

Correspondence

nicolas.minc@ijm.fr (N.M.), delphine.delacour@univ-amu.fr (D.D.)

In brief

Saleh et al. demonstrate that cell division orientation in mouse intestinal epithelium does not follow the localization of canonical polarity cues. They identify a mechanism based on microtubule length limitation that orients spindles in the tissue plane from the apical geometry of mitotic cells.

Saleh et al., 2023, Developmental Cell *58*, 1–15
September 11, 2023
https://doi.org/10.1016/j.devcel.2023.06.004

CellPress

Please cite this article in press as: Saleh et al., Length limitation of astral microtubules orients cell divisions in murine intestinal crypts, Developmental Cell (2023), https://doi.org/10.1016/j.devcel.2023.06.004

Developmental Cell

CellPress

Article

Length limitation of astral microtubules orients cell divisions in murine intestinal crypts

Jad Saleh,[1] Marc-Antoine Fardin,[1,5] Amlan Barai,[1,5] Matis Soleilhac,[1] Olivia Frenoy,[1] Cécile Gaston,[1] Hongyue Cui,[1] Tien Dang,[1] Noémie Gaudin,[1] Audrey Vincent,[2,3] Nicolas Minc,[1,4,*] and Delphine Delacour[1,6,*]
[1]Université Paris Cité, CNRS, Institut Jacques Monod, 75013 Paris, France
[2]Université de Lille, CNRS, INSERM, CHU Lille, UMR9020-U1277, 59000 Lille, France
[3]ORGALille Core Facility, CANTHER, Université de Lille, CNRS, INSERM, CHU Lille, UMR9020-U1277, 59000 Lille, France
[4]Equipe Labellisée La Ligue Contre le Cancer, France
[5]These authors contributed equally
[6]Lead contact
*Correspondence: nicolas.minc@ijm.fr (N.M.), delphine.delacour@univ-amu.fr (D.D.)
https://doi.org/10.1016/j.devcel.2023.06.004

SUMMARY

Planar spindle orientation is critical for epithelial tissue organization and is generally instructed by the long cell-shape axis or cortical polarity domains. We introduced mouse intestinal organoids in order to study spindle orientation in a monolayered mammalian epithelium. Although spindles were planar, mitotic cells remained elongated along the apico-basal (A-B) axis, and polarity complexes were segregated to basal poles, so that spindles oriented in an unconventional manner, orthogonal to both polarity and geometric cues. Using high-resolution 3D imaging, simulations, and cell-shape and cytoskeleton manipulations, we show that planar divisions resulted from a length limitation in astral microtubules (MTs) which precludes them from interacting with basal polarity, and orient spindles from the local geometry of apical domains. Accordingly, lengthening MTs affected spindle planarity, cell positioning, and crypt arrangement. We conclude that MT length regulation may serve as a key mechanism for spindles to sense local cell shapes and tissue forces to preserve mammalian epithelial architecture.

INTRODUCTION

Proliferative monolayered epithelia support the morphogenesis, function, and renewal of many stem cell niches and organs during development and adult life[1,2]. They are characterized by an apico-basal (A-B) polarity and an alignment of mitotic spindles and consequent cell divisions within the tissue planes. These planar divisions position divided daughter cells side by side in the epithelial layer[3–5] to promote tissue monolayered architecture, elongation, and homeostasis[6–8]. Accordingly, a misregulation of spindle planarity has been shown to impair cell positioning and tissue integrity and has been proposed to drive the emergence of dysplasia, hyperplasia, or cancer stem cell populations in stem cell niches[9–14]. To date, however, spindle orientation in epithelia has been best studied in model invertebrates and cultured cell lines, which are amenable to high-resolution live imaging and genetic manipulations of spindle-associated elements[11,14]. In contrast, studying cell division orientation in complex mammalian tissues and organs relevant to human physiology and diseases has been in general hampered by the difficulty of performing advanced imaging in live animal models and by the plausible pleiotropic effects of loss-of-function assays[15]. Therefore, addressing the detailed mechanisms regulating spindle orientation in proliferating mammalian epithelial tissues remains an outstanding open endeavor.

In most animal cells and tissues, mitotic spindles are positioned and oriented by forces and torques generated by their astral microtubules (MTs), pulled by dynein motors. Dynein may be evenly distributed over the cytoplasm or cortex, a situation thought to yield length-dependent MT forces that function to center spindles and align them with the long geometrical axis of the cell[16–18]. Dynein can also be activated at specific sub-cellular cortical polarity domains enriched in dynein activators, including nuclear mitotic apparatus (NuMA) and leucine-glycine-asparagine (LGN), such as during asymmetric divisions[11,19–21]. In tissues, these geometrical and polarity cues often compete to dictate spindle and division positioning[22–25]. For instance, the planar orientation of mitotic spindles in columnar monolayered epithelia is thought to rely on the localization of dynein-regulating polarity complexes at the level of lateral junctions, as well as on a complete mitotic rounding that serves to erase the influence of cell geometry and ensures that short mitotic-phase (M-phase) astral MTs bounded by dynamic instabilities reach the cortex to influence spindle orientation[11,14,22,26,27]. In general, however, how cell-shape changes and MT dynamics and polarity effectors intersect to specify spindle planarity in mammalian epithelia remains poorly defined.

Given its high renewal rate throughout adult life, the intestinal tissue provides a prime model to study cell proliferation and

Please cite this article in press as: Saleh et al., Length limitation of astral microtubules orients cell divisions in murine intestinal crypts, Developmental Cell (2023), https://doi.org/10.1016/j.devcel.2023.06.004

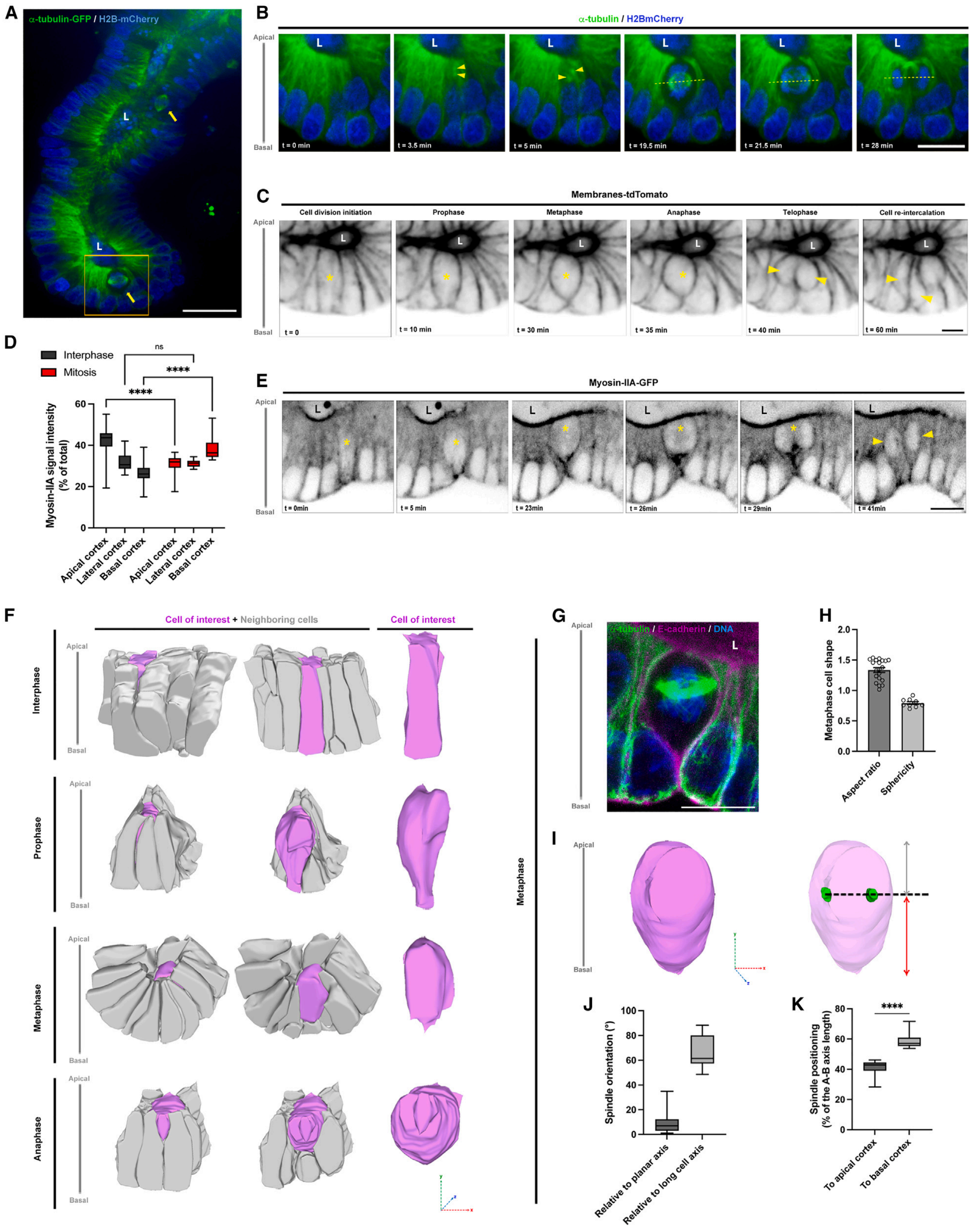

Figure 1. Atypical metaphase cell rounding and spindle orientation in intestinal organoids

(A) Spinning-disk analysis of α-tubulin-GFP (green) and H2B-mCherry (blue) distribution in intestinal crypt organoids. Yellow arrows point on organoid crypt-like structures. L, lumen. Scale bars, 50 μm.

(legend continued on next page)

division in mammals. The surface of the intestine is lined by a monolayer of tall columnar epithelial cells, with mitotic stem and transit-amplifying cells exclusively located in curved tissue invaginations called crypts[28,29]. Previous studies of cell division in the crypt have reported that mitosis is associated with an apical migration of cells and DNA, which ends up with the assembly of a planar spindle in metaphase that specifies cytokinesis orthogonal to the tissue layer[30–34]. However, in part because of the lack of accessibility of the intestine *in vivo*, detailed mechanisms that control planar spindle orientation and the monolayered architecture of the crypt are still lacking.

Here, we build on intestinal organoids to address mechanisms that control division orientation in a 3D mammalian epithelium. Organoids are classically generated from isolated crypts derived from mouse intestinal pieces, and develop regular crypt-like structures with self-renewing capacity within 4 days of culture in 3D hydrogels, thereby mimicking the organization and dynamics of the *in vivo* proliferative compartment[35,36]. Using live 3D imaging, physical, chemical, and genetic interventions, we show that dynein-regulating polarity complexes accumulate at the basal face of mitotic cells and not at lateral junctions and that mitotic cells remain largely elongated along the A-B axis, challenging previous generic models for spindle planarity established in model tissues. We propose a new quantitative model for planar spindle orientation, based on a local apical cell-shape sensing mediated by the length limitation of M-phase astral MTs. This model predicts dose-dependent variations in spindle planarity in normal organoids and in multiple conditions that affect cell shape and polarity.

RESULTS

Mitotic spindles in intestinal crypts orient orthogonal to the cell long axis

The spherical geometry of intestinal organoid crypts grown in 3D provides a unique opportunity to document cell division with optimal optical resolution along the A-B axis of the monolayer. We imaged spindle assembly and positioning along this axis using α-tubulin-GFP/H2B-mCherry organoids (Figure 1A). We confirmed that, as in many columnar epithelia, centrosomes were initially located close to the apical pole during interphase. Centrosomes migrated toward the DNA at the onset of mitosis to assemble prometaphase spindles that initially oscillated to eventually stabilize in metaphase orthogonal to the A-B axis in the tissue plane (Figures 1B, S1A, S1H, and S1I; Videos S1 and S3)[31,33,34]. This planar orientation was maintained throughout metaphase, anaphase, and telophase, yielding cytokinesis that bisected mother cells along the A-B axis and placed daughter cells side by side in the monolayer (Figure 1B; Video S1)[33,34]

To decipher mechanisms that regulate spindle planarity, we first explored the role of cell geometry, which generally orients spindles along the long cell-shape axis[42,43]. We imaged cell contours in live tissues using td-Tomato organoids. This revealed that interphase columnar cells deform at the onset of prophase from the basal pole, yielding an inverted water drop-like metaphase cell shape that is rounder at the apical pole and elongated toward the basal pole (Figures 1C and S1B). These mitotic shape changes were concomitant with a marked basal enrichment of myosin-IIA-GFP as well as P-MLC2, suggesting they are driven by an anisotropic actomyosin-generated cortical tension (Figures 1D, 1E, and S1C–S1F; Video S2). This singular actomyosin distribution may underpin mitotic cell apical migration and neighboring cell rearrangements on the basal side of the epithelium (Figure S1G). In fact, these cell rearrangements around the dividing cell, materialized by the formation of numerous multicellular contacts (3-, 4-, and 5-cell contacts), most likely contributed to maintain tissue cohesion and integrity during division (Figure S1G). Therefore, as previously reported in *Drosophila* imaginal disc[44], but in contrast to many epithelial tissue and adherent cells in which the actomyosin cortex homogeneously remodels to ensure a complete mitotic rounding[22,26,45], metaphase cells remain elongated along the A-B axis in intestinal organoids.

Full 3D reconstitution of confocal tissue z stacks allowed to quantify metaphase cell shapes along with spindle orientations and positions (Figures 1F and S1B). This showed that metaphase cells exhibit a mean aspect ratio of 1.33 ± 0.04 along the A-B

(B) Time-lapse images of α-tubulin-GFP (green) and H2B-mCherry (blue) during mitosis. Yellow arrowheads point on migrating centrosomes. Yellow dotted lines highlight spindle axis. Scale bars, 10 μm.

(C) Time-lapse images of tdTomato organoids showing mitosis progression. Yellow star points on a dividing cell. Yellow arrowheads point on daughter cell separation and re-integration in the epithelial monolayer. Scale bars, 5 μm.

(D) Statistical analysis of the percentage of total signal intensity for myosin-IIA-KI-GFP at the apical, lateral, or basal cortex in interphase (gray) or during mitosis (red). Interphase: myosin-IIA signal intensity at the apical cortex = 41.88% ± 1.38% (mean ± SEM), lateral cortex = 31.6% ± 0.78%, basal cortex = 26.47% ± 0.89%. Mitosis: myosin-IIA signal intensity at the apical cortex = 30.64% ± 0.84% (mean ± SEM), lateral cortex = 31.16% ± 0.28%, basal cortex = 38.26% ± 1.02%. N = 4 experiments, n = 30 cells. Two-way ANOVA test and Sidak's multiple comparison test, ****$p < 0.0001$, ns non-significant.

(E) Time-lapse of a live-imaged cell division in myosin-IIA-KI-GFP organoid crypt. Yellow star points on a dividing cell. Yellow arrowheads point on daughter cell separation and re-integration in the epithelial monolayer. Scale bars, 10 μm.

(F) Representative 3D rendering of a metaphase cell (magenta) and neighboring cells (gray) after segmentation of cell membranes based on confocal z stacks in crypt organoids. Spatial coordinates are shown.

(G) Confocal analysis of α-tubulin (green) and E-cadherin (magenta) distribution in organoid metaphase cells. Scale bars, 10 μm.

(H) Quantitative analyses of the aspect ratio (distance between the spindle axis and the basal membrane over the distance between the spindle axis and the apical membrane) (n = 20 cells) and sphericity (n = 9 cells) of the organoid metaphase cells. Aspect ratio = 1.33 ± 0.04 (mean ± SEM), sphericity = 0.79 ± 0.02.

(I) Representative 3D rendering after segmentation of cell membranes and spindle poles from confocal z stacks of organoid metaphase cells. Cell shape is depicted in magenta and in transparency, spindle poles in green. Distances between the spindle axis (black dotted line) and the apical (gray arrow) or basal membrane (red arrow) are shown. Spatial coordinates are shown.

(J) Statistical analysis of the spindle orientation relative to planar axis (gray) or long cell axis (light gray). Spindle orientation relative to planar axis = 8.61° ± 1.52° (mean ± SEM), to long cell axis = 66.13° ± 3.8°. N = 3 experiments, n(planar axis) = 25 cells, n(long cell axis) = 12 cells.

(K) Statistical analysis of the percentage of the distance between the spindle axis and the apical (gray) or basal (light gray) membrane. Distance from apical membrane = 40.728% ± 1.485% (mean ± SEM), from basal membrane = 59.272% ± 1.485%. N = 3 experiments, n = 13 cells. Paired t test, ****$p < 0.0001$.

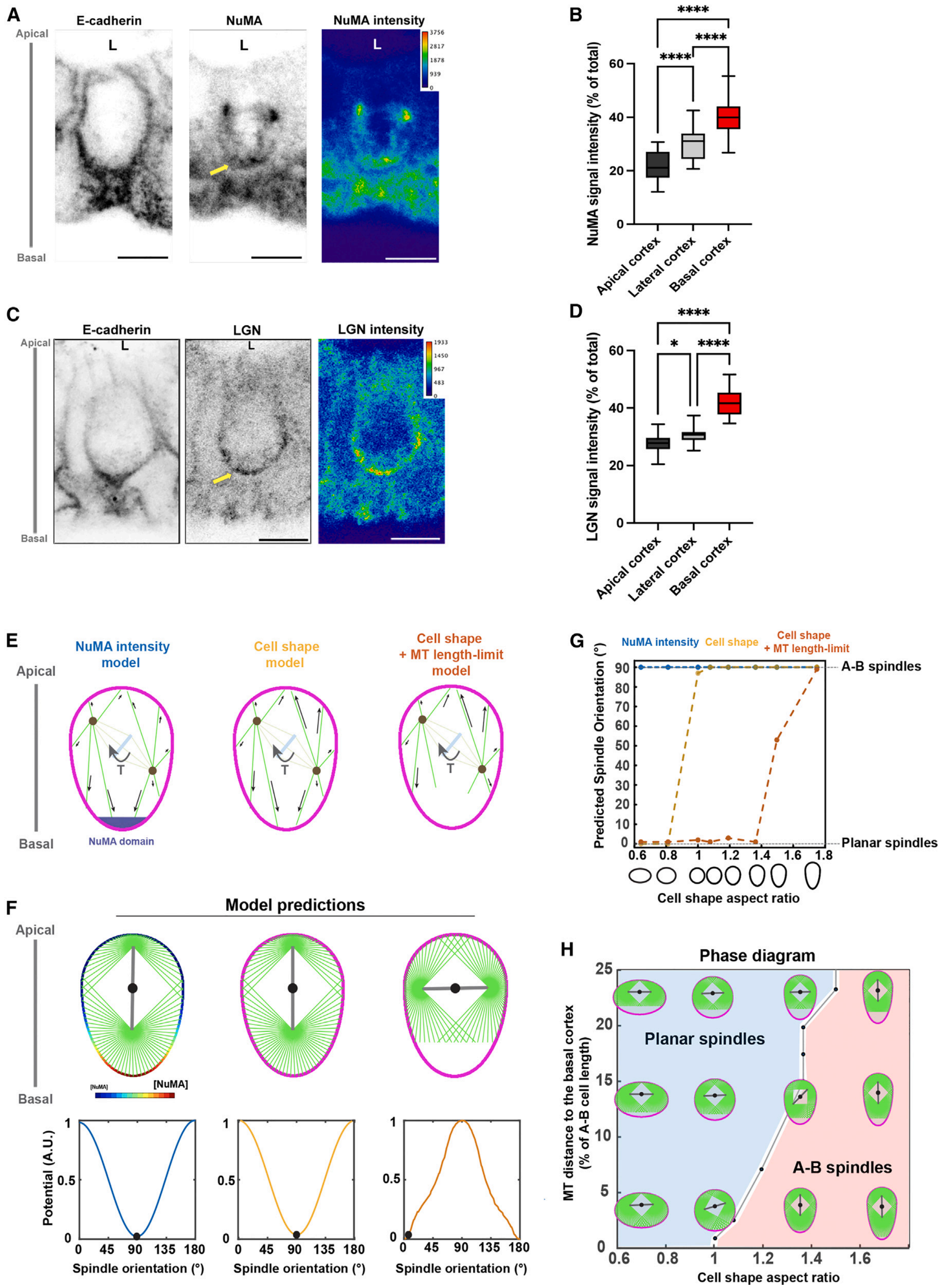

Figure 2. A 2D model for spindle orientation predicts that length limitation in M-phase astral MTs may account for spindle planarity

(A) Confocal analysis of the distribution of E-cadherin and NuMA in mouse organoid metaphase cells. NuMA signal intensity is color-coded with Fire LUT (lookup table) from ImageJ on the right. Color scale bar indicates the gray value intensity. Yellow arrow points to basal accumulation of NuMA. Scale bars, 5 μm.

(legend continued on next page)

Please cite this article in press as: Saleh et al., Length limitation of astral microtubules orients cell divisions in murine intestinal crypts, Developmental Cell (2023), https://doi.org/10.1016/j.devcel.2023.06.004

axis, and a sphericity of 0.79 ± 0.02 (Figures 1G–1I), with a mean angle between mitotic spindles and the cell's long axis of 66.1° ± 3.8° (Figure 1J). In addition, spindles were not centered at the geometrical cell center. Rather, they were shifted asymmetrically at an average position of 40.7% ± 1.5% of the cell's long axis length toward the apical pole (Figures 1G, 1I, and 1K). Importantly, similar elongated mitotic shape, planar, and asymmetrically positioned spindles were observed *in vivo* in crypts of mouse jejunum (Figures S2A–S2D). Therefore, planar cell division in intestinal crypts may not directly follow long-axis geometrical rules, with a spindle oriented nearly orthogonal to the long cell-shape axis and positioned asymmetrically toward the apical cell domain.

Dynein-regulating polarity complexes localize to basal poles of mitotic cells and may not contribute to spindle orientation

These observations prompted us to assay the localization of dynein-associated polarity complexes, which are potential candidates to override geometric guiding cues[3,5,23,25,46,47]. We imaged multiple components of evolutionary conserved polarity complexes, which control spindle orientations in many tissues, including the dynein-regulators NuMA and LGN, as well as the LGN-binding partner afadin[48,49]. During interphase, NuMA was mostly localized within the nucleus and re-located to spindle poles and to the cortex throughout mitosis, as reported in many systems[50,51] (Figure S2E). However, although we expected the cortical pool of NuMA to localize to lateral poles in face of spindle poles, as described in many epithelia and adherent cells[14], it was largely enriched to basal poles of metaphase cells, away from and orthogonal to spindles, in both intestinal organoids and *in vivo* jejunum (Figures 2A, 2B, S2E, and S2F). Similar basal cortical enrichments were found for LGN and afadin (Figures 2C, 2D, S2G, and S2H). Dynein was, in contrast, localized throughout the cytoplasm and cortex and accumulated at spindle poles (Figures S2I and S2J). These data show that canonical polarity complexes are segregated in an unconventional manner, away from lateral cortices and spindle planes in intestinal crypts. Rather, they appear to follow sites with increased cortical and junctional tension, as evidenced by the basal accumulation of the actomyosin cytoskeleton (Figures S1C–S1F) and E-cadherin (Figures S2K–S2N) as previously reported in mammalian cell lines[49,52,53].

To identify potential mechanical designs in astral MT force distributions that orient planar spindles in this tissue, we developed 2D mathematical models. Starting from a series of idealized cell shapes elongated along or orthogonal to the tissue plane, we placed spindles asymmetrically toward the apex, as in experiments, and computed the torque exert generated by astral MTs as a function of spindle orientation to identify rotational equilibrium angles[39,40,54]. As expected, when MTs were grown to fill the whole cell and exert length-dependent forces (shape-sensing system[40]), spindles were oriented along the long cell-shape axis, in the A-B axis of the tissue. Similarly, assuming that astral MT forces were scaled to the amount of the dynein-regulator NuMA[39], also oriented spindles to face NuMA basal domains along the A-B axis (Figures 2E–2G). We conclude that previously established generic models for spindle orientation may not simply account for the observed spindle planarity and that canonical polarity complexes may not influence spindle orientation in this tissue.

Length limitations of M-phase astral MTs promote spindle planarity

Because M-phase astral MT growth and lengths are generally bounded by dynamic instabilities, we tested a model based on a length limitation of astral MTs[55,56]. We reasoned that such limitations could, in principle, prevent astral MTs from reaching basal poles of elongated mitotic cells and create an anisotropy of mitotic aster pair shapes now longer along the planar axis. Remarkably, in 2D models, this limitation coupled to length-dependent MT forces robustly predicted planar spindle orientation for a range of cell shapes and model parameters (Figures 2E–2H and S3A–S3D). Interestingly, however, as cells became too elongated along the A-B axis, spindles eventually turned to a preferred orientation along the long A-B axis, yielding a bi-stable phase diagram controlled by the distance from MT (+)-tips to the basal poles and cell-shape aspect ratio (Figures 2F–2H). These modeling results suggest that a cell-shape-sensing mechanism truncated by a limit in MT length could, in principle, function to orient spindles in the plane of intestinal organoids.

To test this hypothesis, we imaged the distribution of astral MTs around spindles. We implemented expansion microscopy of intestinal organoids to visualize and quantify individual astral MTs. This revealed the presence of astral MT (+)-tips in close contact with both apical and lateral cortices (Figures 3A, 3C,

(B) Statistical analysis of NuMA signal intensity at the apical, lateral, or basal cortex. NuMA signal intensity at the apical cortex = 21.65% ± 1.01% (mean ± SEM), lateral cortex = 29.88% ± 1.01%, basal cortex = 40.65% ± 1.24%. n = 30 cells. One-way ANOVA test and Tukey's multiple comparison test, ****$p < 0.0001$. Three independent experiments were carried out.

(C) Confocal analysis of the distribution of E-cadherin and LGN in human organoid metaphase cells. LGN signal intensity is color-coded with Fire LUT from ImageJ on the right. Color scale bar indicates the gray value intensity. Yellow arrow points to basal accumulation of LGN. Scale bars, 5 μm.

(D) Statistical analysis of LGN signal intensity at the apical, lateral, or basal cortex. LGN signal intensity at the apical cortex = 27.86% ± 0.57% (mean ± SEM), lateral cortex = 30.41% ± 0.45%, basal cortex = 41.77% ± 0.79%. n = 30 cells. One-way ANOVA test and Tukey's multiple comparison test, *$p = 0.012$, ****$p < 0.0001$. Three independent experiments were carried out.

(E) Schemes representing the core hypothesis of the distribution of microtubule (MT) length and polarity domains in the 3 tested models for spindle orientation.

(F) Rotational potential energy profiles plotted as a function of spindle orientation angles with respect to the planar axis predicted by the 3 different models. The black dot marks the preferred spindle orientation at the minimum of the potential profiles.

(G) Predicted preferred spindle orientation for a range of cell shapes with increasing aspect ratios in the tissue plane or along the A-B axis. Note how the model based on cell shape coupled to length limitation in MTs transits from predicting planar spindles to A-B-oriented spindles when cells become over-elongated, along the A-B axis.

(H) Phase diagram of the predicted preferred spindle orientations for the model based on cell shape and a limit in MT lengths, drawn as a function of the 2 control parameters, the distance of MT- (+) tips to the basal side and the elongation of mitotic cell shapes.

Please cite this article in press as: Saleh et al., Length limitation of astral microtubules orients cell divisions in murine intestinal crypts, Developmental Cell (2023), https://doi.org/10.1016/j.devcel.2023.06.004

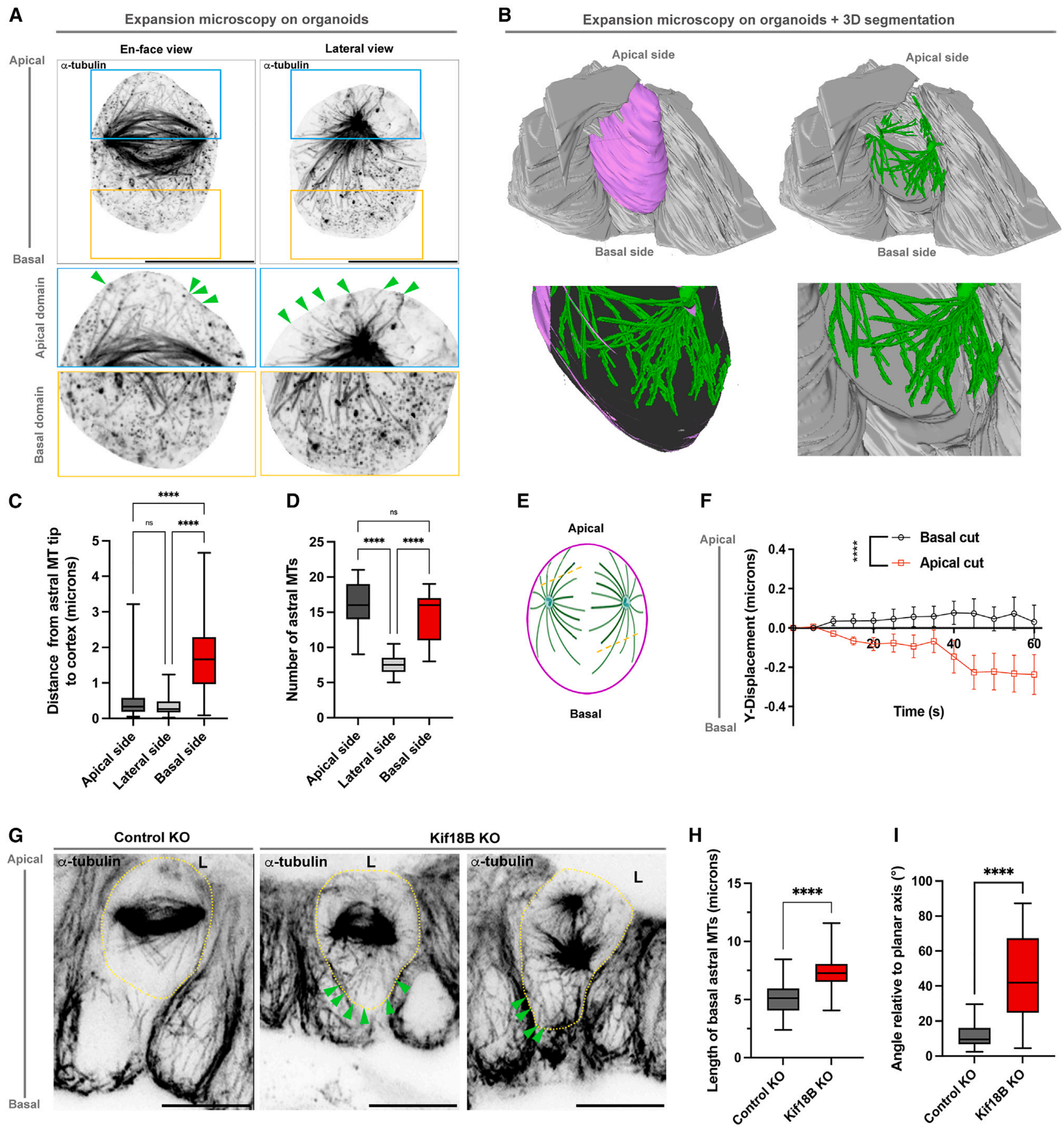

Figure 3. Existence of a length limit for M-phase astral MTs that impact spindle orientation

(A) Projected confocal z stacks of α-tubulin distribution in isolated organoid metaphase cells. En-face and lateral views are presented. Apical domain areas boxed in blue and basal domain areas boxed in yellow are presented in the low. Green arrowheads point to astral MTs contacting the apical cortex. Corrected scale bars, 10 μm.

(B) Representative 3D rendering of a metaphase cell (magenta), neighboring cells (gray), spindle poles, and microtubules (green) after segmentation of a confocal z stack of E-cadherin and α-tubulin localization. Are depicted A-B views tilted to show basal cortex.

(C) Statistical analysis of the distance between the astral MT tip and the apical, lateral, or basal cortex. Distance between astral MT tip and the apical cortex = 0.466 ± 0.045 μm (mean ± SEM), the lateral cortex = 0.349 ± 0.025 μm, the basal cortex = 1.685 ± 0.086 μm. Three experiments were carried out. 11 cells were analyzed. n = 104 apical astral MTs, n = 102 lateral astral MTs, n = 107 basal astral MTs. Two-way ANOVA with Tukey's multiple comparisons test, ****$p < 0.0001$; ns, non-significant.

(D) Statistical analysis of the number of astral MTs at the apical, lateral, and basal sides. Number of astral MTs at the apical side = 16.3 ± 1.09 (mean ± SEM), at the lateral side = 7.6 ± 0.5, at the basal side = 14.2 ± 1.06. Three experiments were carried out and 11 cells were analyzed. Unpaired t test, ****$p < 0.0001$; ns, non-significant.

(legend continued on next page)

and S3E–S3G). In sharp contrast, MTs were barely detected in contact with the basal side, with MT (+)-tips located at a distance ~4× higher on average from the basal cortex than the apical one (Figures 3A–3C, S3E, and S3H). Importantly, these effects were not caused by a putative anisotropy in MT nucleation because the number of MTs growing apically vs. basally was similar (Figure 3D). In addition, imaging of the (+)-tip-associated protein EB3-GFP confirmed this exclusion in live tissues (Figure S3I; Video S3). To further test this differential MT-cortex interaction, we performed laser severing of groups of MTs in α-tubulin-GFP organoids along a line-scan orthogonal to the A-B axis, placed either on the apical or basal side of spindles (Figures 3E, 3F, S3J, and S3K). Both caused spindle recoils away from the cuts, suggesting that astral MTs predominantly exert pulling forces, presumably by engaging with dynein motors at the cortex[57,58]. However, in agreement with the lesser extent of MTs reaching the basal cortex, basal cuts caused significantly smaller recoils than apical ones (Figures 3F and S3K). These data further support an asymmetry in MT-cortex contacts along the A-B axis and a lack of contribution from basal polarity cues to MT forces and spindle orientation.

To directly assay the role of MT length regulation, we next sought to increase astral MTs length and monitor impact on spindle orientation. Kif18B, an important (+)-tip depolymerizing kinesin, was shown to promote MT catastrophe and thus limit the length of M-phase astral MTs in mammalian cells and tissues[56,59]. Interestingly, in intestinal organoids, we found that Kif18B accumulated at the basal domain of metaphase cells, colocalizing with polarity cues, as observed in other cell types and tissues (Figures S3L–S3N)[60]. This observation suggests that Kif18B could promote MT depolymerization from the basal side to limit MT length. Accordingly, knocking out Kif18B using a CRISPR-Cas9 inducible system in organoids led to significantly longer astral MTs, with basal-facing MTs that now grew long enough to reach the cell cortex (Figures 3G, 3H, S3O, and S3P).

Strikingly, mitotic spindles in Kif18B-KO organoids were not planar anymore and rather oriented randomly, with a significant fraction of spindles oriented along the A-B axis (Figure 3I). Importantly, shortening back astral MTs using a low-dose nocodazole treatment in Kif18B-KO organoids restored planar spindle orientation (Figures S3Q and S3R), suggesting that spindle orientation defects in this mutant may be primarily associated with a misregulation of MT length. Finally, in Kif18B-KO organoids, NuMA was no longer accumulated at the basal cortex but dispersed in multiple patches around the cell surface, yet still away from spindle poles, reinforcing the lack of direct contribution of polarity effectors to spindle orientation in this tissue (Figures S3S and S3T). Together, these results suggest that a length limitation of basal mitotic astral MTs, mediated in part by depolymerizing kinesins, may prevent MTs from interacting with basal polarity factors and allow spindles to orient in the tissue plane by probing the geometry of the apical fraction of dividing cells.

A 3D model for spindle position and orientation in intestinal crypts

In order to test further the length-limitation hypothesis, we explored the parameter space in the model phase diagram (Figures 2F–2H) by experimentally altering cell shapes. We first elongated cells in the tissue plane to validate the general influence of apical cell shape. We grew organoids in L-WNR (L cell line secreting Wnt3a, R-spondin and Noggin) conditioned medium, an exogenous global Wnt3a treatment that results in the formation of hyper-proliferative and undifferentiated cystic structures[61,62], in which the epithelial monolayer displays a flat squamous morphology with cells now elongated in the tissue plane (Figure S4A). As predicted by models, and not surprisingly, spindles are oriented parallel to the long cell-shape axis in the tissue plane in this condition (Figures 4A–4D and S4A). To increase mitotic cell elongation along the A-B axis, we next affected contractility by inhibiting myosin-IIA activity. Both blebbistatin treatment and myosin-IIA-KO drastically impaired mitotic shape changes and rounding, with cells remaining significantly more elongated along the A-B axis than controls (Figures 4A–4C and S4B–S4E). This resulted from a loss of cellular rearrangements and the formation of fewer multicellular contacts in the basal environment of metaphase cells (Figures S4D–S4H). These results confirmed the primary function of basal actomyosin contractility in reshaping mitotic cells and its contacts with neighbors in this tissue. Importantly, as predicted in models (Figures 2F and 2H), in these more A-B elongated metaphase cells, spindle orientation was not planar anymore, with many cells aligning their spindles closer to the A-B axis (Figures 4A, 4B, and 4D). Importantly, in these conditions, polarity complexes detached from the cell cortex (Figures S4I and S4J) and spindles were still positioned off-center toward the apical cell poles (Figure 4B), ruling out here again any putative contributions of basal polarity to spindle orientation.

To test our hypothesis about these conditions affecting cell shapes using realistic 3D cell geometries, we next turned to simulations. We adapted a gradient descent strategy that can predict both spindle orientation and position in 3D from the 3D geometry of mitotic cells, the localization of polarity cues, and length limitation in astral MTs[25]. Using 3D segmentations of individual cell contours, spindle poles, and basal domains from fixed tissues, we reconstituted experimental cell shapes, polarity, and spindle orientation and position in mitotic cells (Figure 4E). By inputting the experimental geometry and a limit for MT growth at the basal pole in the model to account for Kif18B enrichment there, we ran simulations starting from random positions and orientations and searched for equilibrium. The simulations were robust to initial conditions and predicted with accuracy in 3D the planarity of spindles

(E) Scheme showing the position of apical or basal laser cut (yellow dotted lines) of astral MTs.

(F) Statistical analyses of the spindle pole displacement in the y axis after apical or basal laser cut in organoid metaphase cells. 6 cells were analyzed for each condition. Unpaired t test, ****$p < 0.0001$.

(G) Confocal analysis of α-tubulin distribution in metaphase cells in control-KO or Kif18B-KO organoids. Yellow dotted line delimits the metaphase cell. Green arrowheads point to astral MTs contacting the basal cortex. L, lumen. Scale bars, 10 μm.

(H) Statistical analysis of the length of basal astral MTs in metaphase cells of control-KO or Kif18-KO organoids. n = 99 astral MTs in 13 control-KO cells, n = 103 astral MTs in 17 Kif18-KO cells. Unpaired t test, ****$p < 0.0001$.

(I) Statistical analysis of the spindle axis orientation relative to the planar axis of the epithelium in metaphase cells of control-KO or Kif18-KO organoids. n = 32 control-KO cells, n = 50 Kif18-KO cells. Unpaired t test, ****$p < 0.0001$. For each experiment, three independent experiments were carried out.

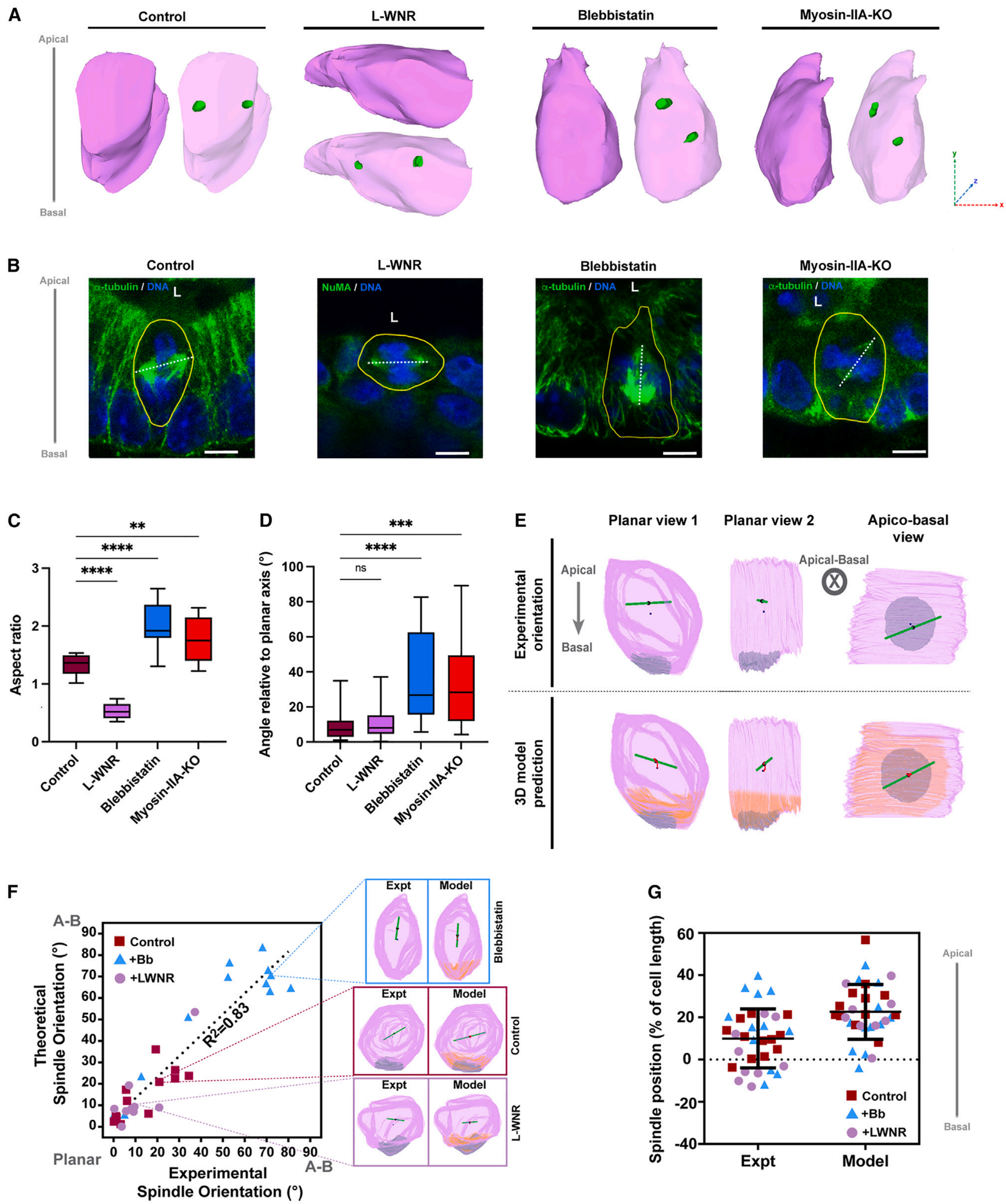

Figure 4. Metaphase cell shape impacts planar spindle orientation in organoid cells

(A) Representative 3D rendering of cell shape and spindle pole positioning after segmentation of cell membranes and NuMA spindle-associated signal from confocal z stacks of control (DMSO-treated), L-WNR-cultured, blebbistatin-treated, or induced myosin-IIA-KO organoid metaphase cells. Cell shape is depicted in magenta, spindle poles in green. Spatial coordinates are shown.

(legend continued on next page)

Please cite this article in press as: Saleh et al., Length limitation of astral microtubules orients cell divisions in murine intestinal crypts, Developmental Cell (2023), https://doi.org/10.1016/j.devcel.2023.06.004

and their apical shifts in control and L-WNR, as well as their reorientation along the A-B axis in more elongated blebbistatin-treated cells (Figures 4E–4G and S5A–S5C; Videos S4 and S5). In contrast, models in which astral MTs filled whole-cell volumes or models based on a predominant influence of NuMA domains yielded poor agreements with experiments (Figures S5D–S5G). Importantly, the model predicted deviations from planarity in a dose-dependent manner among more or less elongated WT or blebbistatin-treated cells and also the correct orientation of spindles within the tissue plane when shape anisotropies were present in this plane (Figures 4E and 4F). These direct comparisons between 3D model predictions and experiments strongly support the idea that length limitations of astral MTs can account for spindle position and planar orientation in intestinal crypts.

Lengthening astral MTs affect epithelial tissue layering

This truncated shape sensing may have many advantages for the regulation of tissue layering and cell density. For instance, it may allow cells to adapt division orientation to planar tissue forces, tilting spindles along the A-B axis if cells become over-compressed by their neighbors, providing a potential homeostatic mechanism to regulate cell density and monolayered architecture[17]. Accordingly, in Kif18B-KO organoids, as a consequence of spindle misorientation, planar polarity of cytokinesis and placement of daughter cells were largely impaired (Figures 5A and 5B). Hence, the regular basal nuclear arrangement, which is a hallmark of polarized columnar epithelia, was lost 3 days after KO induction (Figures 5A, 5C, and 5D). Finally, nuclei densities were significantly reduced in the Kif18B-KO (Figure 5E), showing how spindle misorientation may impact crypt architecture and cell density. These results directly demonstrate how a modulation in astral MT length may impact spindle planarity and the architecture of a mammalian tissue.

DISCUSSION

A new model for planar spindle orientation in proliferative epithelia

How spindle orientation is regulated in proliferative tissues and stem cell niches is of fundamental importance for organ morphogenesis and homeostasis and is highly relevant to human disorders[10,44,63,64]. Here, by documenting with high temporal and spatial resolution spindle orientation together with MT dynamics, cell shape, and polarity in a 3D mammalian proliferative organoid, we propose a new model for the control of planar spindle orientation and monolayered tissue architecture. This model is based on partial cell-shape sensing resulting from length limitation of M-phase astral MTs, mediated by an enrichment of depolymerizing promoting factors at the basal pole. This limitation is thus coupled to the A-B polarity of the columnar tissue and allows initially apically positioned centrosomes to stop their basal migration at a position shifted toward the apex and astral MTs to probe the local apical fraction of mitotic cells to orient spindles in the tissue plane (Figures 5F, S5H, and S5K). This mechanism has similarities with previous models proposed for asymmetric aster pair positioning and orientation in some large zygotes featuring anisotropic MT asters[25,65] (Figure 5F). Importantly, our model contrasts with established ones in many epithelia, in which the role of polarity effectors, including NuMA, LGN, or afadin recruited to lateral cortices, is thought to be predominant to orient spindles in the tissue plane[14]. In intestinal crypts, their unconventional localization to the basal domain of mitotic cells suggests that they may not contribute to orient spindles and raises the question of how they may be segregated there.

We found that both myosin-IIA and Kif18B inhibition affected their localization at the basal cortex (Figures S3S, S3T, S4I, and S4J). Therefore, we suggest that basal polarity recruitment could be in part driven by enhanced local cortical tension associated with basal actomyosin activity and cellular rearrangements (Figures 1D, 1E, and S1A–S1G), as proposed in *Drosophila*[39] or epithelial cell lines[49,52,53] or by yet unknown mechanisms mediated by Kif18B or MT-(+) tip contacts[60]. Other plausible mechanisms contributing to this basal localization might include a local clearance of polarity effectors from the apex from chromosome-derived signals[66,67] or a recruitment associated with the numerous basal multicellular contacts formed in mitosis[39].

Interestingly, asymmetric actomyosin activity in other epithelial cells and tissues has been proposed to directly influence spindle orientation. In *Drosophila*, one study notably reported that local actomyosin enrichment may override geometrical

(B) In control (DMSO-treated), L-WNR-cultured, blebbistatin-treated, or induced myosin-IIA-KO organoid metaphase cells, the confocal image of α-tubulin or NuMA (green) and nuclei (blue). Scale bars, 5 μm.

(C) Statistical analyses of organoid metaphase cell aspect ratio in control (DMSO-treated), L-WNR-cultured, blebbistatin-treated, or induced myosin-IIA-KO organoid metaphase cells. Aspect ratio of metaphase cells in control organoids = 1.33 ± 0.04 (mean ± SEM), in L-WNR-cultured organoids = 0.53 ± 0.04, in blebbistatin-treated organoids = 2.01 ± 0.12, in myosin-IIA-KO organoids = 1.78 ± 0.13. n(control organoids) = 20 cells, n(L-WNR organoids) = 10 cells, n(blebbistatin-treated organoids) = 10 cells, n(myosin-IIA-KO organoids) = 10 cells. One-way ANOVA, with Tukey's multiple comparisons tests, **p = 0.0011, ****p < 0.0001.

(D) Statistical analyses of the spindle axis orientation relative to the plane of the epithelium. Angle deviation in control organoids = 8.61° ± 1.52° (mean ± SEM), in L-WNR-cultured organoids = 11.28° ± 3.74°, in blebbistatin-treated organoids = 37.11° ± 5.04°, in myosin-IIA-KO organoids = 34.88° ± 5.22°. n(control organoids) = 25 cells, n(L-WNR organoids) = 9 cells, n(blebbistatin-treated organoids) = 25 cells, n(myosin-IIA-KO organoids) = 25 cells. One-way ANOVA, ***p = 0.0001, ****p < 0.0001. ns, non-significant. For each experiment, three independent experiments were carried out.

(E) (Top) 3D reconstitution of experimental cells obtained from 3D z stacks of a representative dividing cell labeled for E-cadherin and NuMA to extract cell shape (magenta), spindle orientation (green line), and NuMA accumulation at the basal cortex (gray domain). (Bottom) Corresponding simulation output, based on MT length-dependent forces (shape sensing) and an exclusion of MTs length in the basal domain region (orange zone). The red traces represent the history of spindle axis displacement in the simulation. Both experimental and simulated cells are viewed in different planes with respect to A-B axis.

(F) Predicted spindle orientation angle with respect to the A-B axis, plotted as a function of the experimental axis for 10 individual control, L-WNR-treated, or blebbistatin-treated crypt cells. Insets provide representative examples of experimental and simulated spindle orientation in the different treatments. The dotted line is a linear fit, with a slope of 0.96 (1 being a perfect agreement between models and experiments). R^2 is the correlation coefficient between the fit and the data. Expt, experimental.

(G) Experimental and theoretical prediction of spindle asymmetric position toward the apical cell poles in the indicated conditions.

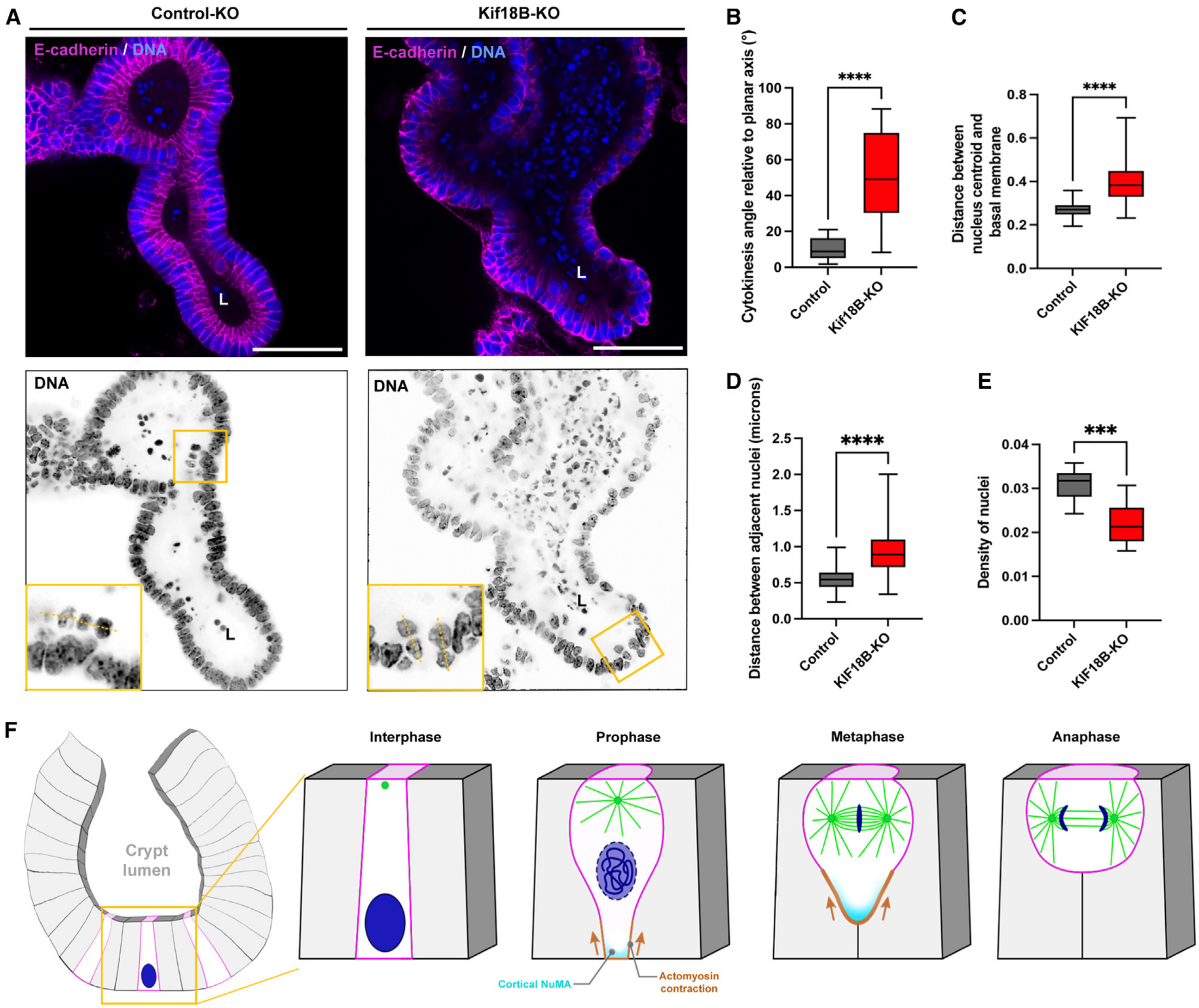

Figure 5. Impact of spindle misorientation in epithelial organization

(A) Confocal microscopy analysis of the distribution of the E-cadherin (magenta) and nuclei (blue) in control-KO and Kif18B-KO organoids. Representative cytokinesis events are boxed in yellow and presented in bottom left. Yellow dotted lines highlight cell division axis. L, lumen. Scale bars, 50 μm.

(B) Statistical analysis of cytokinesis angle relative to the planar axis in control-KO or Kif18B-KO organoids. n = 13 control-KO cells, n = 26 Kif18B-KO cells. Cytokinesis angle (control-KO) = 10.3° ± 1.68°, cytokinesis angle (Kif18B-KO) = 50.8° ± 4.9°. Unpaired t test, ****$p < 0.0001$.

(C) Statistical analysis of interphase nuclear positioning (distance from the centroid of the interphase nucleus to the basal membrane) (n = 100 cells). Nuclear positioning (control-KO) = 0.271 ± 0.003 μm (mean± SEM), (Kif18B-KO) = 0.399 ± 0.01 μm. Unpaired t test, ****$p < 0.0001$.

(D) Statistical analysis of distance between adjacent interphase nuclei (n = 100 cells). Distance between nuclei (control-KO) = 0.559 ± 0.015 μm (mean ± SEM), (Kif18B-KO) = 0.939 ± 0.032 μm. Unpaired t test, ****$p < 0.0001$.

(E) Statistical analysis of nucleus density (n = 10 fields). Nucleus density (control-KO) = 0.031 ± 0.001 μm (mean ± SEM), (Kif18B-KO) = 0.022 ± 0.001 μm. Unpaired t test, ***$p = 0.0002$.

(F) Scheme depicting the proposed model of spindle polarity modulation in organoid metaphase cells.

cues to orient spindles in the face of actomyosin-rich zones[68]. In cultured cells, a recent local optogenetic assay showed the opposite behavior, with spindles orienting orthogonal to the most contractile cortical zone[69]. Our findings in the crypt align more with this latter finding, at least in terms of geometrical outputs. However, our results favor a more indirect role for basal actomyosin asymmetric enrichment, primarily impacting spindle orientation through its role in controlling mitotic cell-shape changes. We currently do not understand which mechanism may enrich actomyosin at the basal poles of mitotic crypt cells. We suggest it may reflect the need for apical migrations of dividing cells in columnar tissues, as proposed in the mouse nervous system or zebrafish retina[70,71]. Furthermore, actomyosin is not only enriched at the base of the metaphase cell but also in its direct neighbors, together with E-cadherin and afadin (Figures S1C–S1F and S2G–S2L). This basal actomyosin pool may promote multi-junctional remodeling and cell cohesion, as proposed in other contexts[72,73], given the lack of multicellular

Please cite this article in press as: Saleh et al., Length limitation of astral microtubules orients cell divisions in murine intestinal crypts, Developmental Cell (2023), https://doi.org/10.1016/j.devcel.2023.06.004

contacts and basal neighbor cell remodeling when myosin is inhibited in organoids (Figures S4E–S4H).

Length regulation of M-phase MTs, mitotic rounding, and spindle orientation

Astral MTs control spindle positioning in organisms ranging from yeast to mammals[16]. Although most models have thus far largely assumed that astral MTs grow to reach the cortex, to probe cell shapes and polarities, recent studies have suggested that M-phase astral MTs, which are bounded by dynamic instabilities, may be just long enough in mitosis to reach the cortex of fully rounded cells[74]. Accordingly, impairment of mitotic rounding can prevent MTs from properly interacting with the cortex, leading to chromosome segregation and spindle orientation defects[26,75]. In intestinal organoids, using live imaging and expansion microscopy, we found that astral MTs rarely reach the basal domain of the metaphase cell. Based on these observations, we propose that this cell-cycle-regulated length limitation may be exploited in the organoid tissue to allow the spindle to only probe apical cell shapes, position asymmetrically, and orient in the tissue plane. In support of this, we found that Kif18B, a MT-depolymerizing kinesin that limits astral MT length in numerous mammalian cell lines and primary cultures[56,59,60], localizes to the basal pole of metaphase cells in intestinal organoids (Figures S3M and S3N). Loss of Kif18B does not disrupt initial apical centrosome migration (Figures S5H, S5J, and S5K) but leads to significantly longer MTs and random spindle orientation (Figures 3G–3I). Therefore, although we cannot fully discard a more indirect mechanism by which Kif18B could regulate spindle orientation, we propose it may primarily function to negatively regulate MT growth to allow spindles to probe local apical shapes.

In addition to Kif18B, local modulation of MT dynamics or dynein activity could also emerge directly from enhanced basal actomyosin activity or from putative higher basal organelle crowding, as proposed in other systems[25,76,77]. Although the impact of cell shape on division orientation was first reported more than 150 years ago[78], mechanisms by which geometries are being sensed in multicellular tissues are still in their infancy[18]. Our study provides an important new generic mechanism to orient spindles along the short axis in monolayered mammalian epithelia and calls for a better exploration of mechanisms regulating astral MT length and mitotic shape changes in multicellular tissues.

Functions of planar divisions for crypt dynamics and architecture

Planar cell divisions are key for maintaining the monolayered architecture of certain epithelial tissues. Conversely, programmed alterations of planar divisions along the A-B axis of the tissue are required for epithelial stratification, such as during skin development in the mouse embryo[79,80]. In the curved 3D geometry of intestinal crypts, we found that cell divisions orient parallel to the local plane of curvature of the tissue. We propose that such organization of cell divisions may contribute to promoting a near-isotropic expansion of the crypt tip while maintaining a regular monolayered architecture. Accordingly, altering spindle planarity in Kif18B-KO resulted in misplaced daughter cells, often protruding into the apical lumen (Figures 5A–5E). However, beyond its primary conserved function in negatively regulating M-phase MT lengths, Kif18B has also recently been proposed to play a role in the DNA damage response[81]. Therefore, in addition to its spindle orientation regulatory role, we cannot fully exclude other Kif18B functions in maintaining tissue architecture.

Whether such spindle orientation defects could lead to the long-term formation of tumor masses, epithelial dysplasia, or hyperplasia, or if mechanisms such as apoptosis or daughter cell re-integration may safeguard the intestinal tissue, remains to be tested with additional genetic manipulations[82]. In addition, many of the dividing cells in the crypt are Lgr5$^+$-stem cells, which may undergo symmetric fate divisions for self-renewal or asymmetric divisions to generate a daughter cell that becomes fated. As such, whether alteration of planar spindle positioning affects the auto-renewal properties of organoids and their homeostasis, as previously described, for instance, in adenomatous polyposis coli (Apc)-mutated intestinal tissues, is another important open question[83,84]. More work on the regulation and function of oriented division in mammalian stem cell niches, tissues, and organs may help to better appreciate the emergence of human epithelial disorders.

Limitations of the study

Our study establishes a new mechanism for planar spindle orientation based on a limitation of MT length, presumably independent of canonical polarity cues, including LGN and NuMA. This model derives from the unconventional localization of these factors on the basal side of intestinal dividing cells, away from lateral cortices and spindle poles. However, in the present study, we do not address the detailed mechanisms that promote this atypical localization or the general function of polarity cues. This would require the generation of fluorescent knockins, optogenetic tools, or proper loss-of-function alleles, which we failed to generate due to technical difficulties in transfecting this primary culture. Another limitation is that we do not currently understand if the spindle orientation mechanism that we propose is specific to intestinal crypts or mammalian epithelia or if it emerges from the particular topology, dynamics, and mechanics of the tissue.

STAR★METHODS

Detailed methods are provided in the online version of this paper and include the following:

- KEY RESOURCES TABLE
- RESOURCE AVAILABILITY
  - Lead contact
  - Materials availability
  - Data and code availability
- EXPERIMENTAL MODEL AND SUBJECT DETAILS
  - Organoid cultures and transfection
- METHOD DETAILS
  - Antibodies and reagents
  - Drug treatments
  - Biochemical analysis
  - Immunostaining
  - Live imaging

- ○ Laser ablation experiments
- ○ Two-dimensional models for spindle orientation
- ○ Three-dimensional simulations for spindle position and orientation
- ○ Segmentation and 3D rendering
- ○ Expansion microscopy of organoids
- QUANTIFICATION AND STATISTICAL ANALYSIS

SUPPLEMENTAL INFORMATION

Supplemental information can be found online at https://doi.org/10.1016/j.devcel.2023.06.004.

ACKNOWLEDGMENTS

We thank René-Marc Mège and Benoit Ladoux (Institut Jacques Monod, IJM) for helpful discussions, Paula Martin Gil, Valeria Rocchi, and Jeremy Sallé (IJM) for technical help, as well as Yohanns Bellaiche (Institut Curie) for reading the manuscript. We thank Renata Basto, Ana-Maria Lennon-Dumenil, Robert S. Adelstein, and Danijela Vignjevic for providing mice. Confocal microscopy and spinning-disc analyses were performed in the ImagoSeine Microscopy Facility (IJM). This work was supported by grants from the Groupama Foundation—Research Prize for Rare Diseases 2017 (to D.D.), the Fondation pour la Recherche Médicale (FRM) (to C.G.), the Fondation ARC (to J.S.), the Human Frontier Science Program (RGP0038/2018) (to D.D.), the LabEx "Who Am I?" #ANR-11-LABX-0071, and the Université de Paris IdEx #ANR-18-IDEX-0001 funded by the French Government through its "Investments for the Future" program (to N.M. and D.D.), the INCA PLBIO20-150, Cancéropole Ile-de-France (to N.M. and D.D.), La Ligue Contre le Cancer (EL2021.LNCC, to N.M.), the ANR-20-CE13-0015 (to D.D.), and the Fondation Bettencourt Schueller ("Coup d'élan prize") (to N.M.).

AUTHOR CONTRIBUTIONS

J.S., M-A.F., A.B., M.S., O.F., C.G., T.D., H.C., N.M., and D.D. performed experiments. N.M. designed and performed models and simulations. J.S., M-A.F., A.B., C.G., N.M., and D.D. designed the experiments. J.S., M-A.F., A.B., C.G., M.S., H.C., N.M., and D.D. performed analyses. J.S., N.M., and D.D. coordinated the overall research and experiments and wrote the manuscript.

DECLARATION OF INTERESTS

The authors declare no competing interests.

Received: May 24, 2022
Revised: May 25, 2023
Accepted: June 14, 2023
Published: July 6, 2023

REFERENCES

1. Macara, I.G., Guyer, R., Richardson, G., Huo, Y., and Ahmed, S.M. (2014). Epithelial homeostasis. Curr. Biol. *24*, R815–R825. https://doi.org/10.1016/j.cub.2014.06.068.
2. Godard, B.G., and Heisenberg, C.P. (2019). Cell division and tissue mechanics. Curr. Opin. Cell Biol. *60*, 114–120. https://doi.org/10.1016/j.ceb.2019.05.007.
3. Morin, X., Jaouen, F., and Durbec, P. (2007). Control of planar divisions by the G-protein regulator LGN maintains progenitors in the chick neuroepithelium. Nat. Neurosci. *10*, 1440–1448. https://doi.org/10.1038/nn1984.
4. Aigouy, B., Farhadifar, R., Staple, D.B., Sagner, A., Röper, J.C., Jülicher, F., and Eaton, S. (2010). Cell flow reorients the axis of planar polarity in the wing epithelium of Drosophila. Cell *142*, 773–786. https://doi.org/10.1016/j.cell.2010.07.042.
5. Peyre, E., Jaouen, F., Saadaoui, M., Haren, L., Merdes, A., Durbec, P., and Morin, X. (2011). A lateral belt of cortical LGN and NuMA guides mitotic spindle movements and planar division in neuroepithelial cells. J. Cell Biol. *193*, 141–154. https://doi.org/10.1083/jcb.201101039.
6. da Silva, S.M., and Vincent, J.P. (2007). Oriented cell divisions in the extending germband of Drosophila. Development *134*, 3049–3054. https://doi.org/10.1242/dev.004911.
7. Campinho, P., Behrndt, M., Ranft, J., Risler, T., Minc, N., and Heisenberg, C.P. (2013). Tension-oriented cell divisions limit anisotropic tissue tension in epithelial spreading during zebrafish epiboly. Nat. Cell Biol. *15*, 1405–1414. https://doi.org/10.1038/ncb2869.
8. Mao, Y., Tournier, A.L., Hoppe, A., Kester, L., Thompson, B.J., and Tapon, N. (2013). Differential proliferation rates generate patterns of mechanical tension that orient tissue growth. EMBO J. *32*, 2790–2803. https://doi.org/10.1038/emboj.2013.197.
9. Quyn, A.J., Appleton, P.L., Carey, F.A., Steele, R.J., Barker, N., Clevers, H., Ridgway, R.A., Sansom, O.J., and Näthke, I.S. (2010). Spindle orientation bias in gut epithelial stem cell compartments is lost in precancerous tissue. Cell Stem Cell *6*, 175–181. https://doi.org/10.1016/j.stem.2009.12.007.
10. McCaffrey, L.M., and Macara, I.G. (2011). Epithelial organization, cell polarity and tumorigenesis. Trends Cell Biol. *21*, 727–735. https://doi.org/10.1016/j.tcb.2011.06.005.
11. Morin, X., and Bellaïche, Y. (2011). Mitotic spindle orientation in asymmetric and symmetric cell divisions during animal development. Dev. Cell *21*, 102–119. https://doi.org/10.1016/j.devcel.2011.06.012.
12. Bergstralh, D.T., and St Johnston, D. (2014). Spindle orientation: what if it goes wrong? Semin. Cell Dev. Biol. *34*, 140–145. https://doi.org/10.1016/j.semcdb.2014.06.014.
13. Xiong, F., Ma, W., Hiscock, T.W., Mosaliganti, K.R., Tentner, A.R., Brakke, K.A., Rannou, N., Gelas, A., Souhait, L., Swinburne, I.A., et al. (2014). Interplay of cell shape and division orientation promotes robust morphogenesis of developing epithelia. Cell *159*, 415–427. https://doi.org/10.1016/j.cell.2014.09.007.
14. di Pietro, F., Echard, A., and Morin, X. (2016). Regulation of mitotic spindle orientation: an integrated view. EMBO Rep. *17*, 1106–1130. https://doi.org/10.15252/embr.201642292.
15. Donà, F., Eli, S., and Mapelli, M. (2022). Insights into mechanisms of oriented division from studies in 3D cellular models. Front. Cell Dev. Biol. *10*, 847801. https://doi.org/10.3389/fcell.2022.847801.
16. McNally, F.J. (2013). Mechanisms of spindle positioning. J. Cell Biol. *200*, 131–140. https://doi.org/10.1083/jcb.201210007.
17. Wyatt, T.P., Harris, A.R., Lam, M., Cheng, Q., Bellis, J., Dimitracopoulos, A., Kabla, A.J., Charras, G.T., and Baum, B. (2015). Emergence of homeostatic epithelial packing and stress dissipation through divisions oriented along the long cell axis. Proc. Natl. Acad. Sci. USA *112*, 5726–5731. https://doi.org/10.1073/pnas.1420585112.
18. Haupt, A., and Minc, N. (2018). How cells sense their own shape - mechanisms to probe cell geometry and their implications in cellular organization and function. J. Cell Sci. *131*, jcs214015. https://doi.org/10.1242/jcs.214015.
19. Schaefer, M., Shevchenko, A., Shevchenko, A., and Knoblich, J.A. (2000). A protein complex containing Inscuteable and the Galpha-binding protein Pins orients asymmetric cell divisions in Drosophila. Curr. Biol. *10*, 353–362. https://doi.org/10.1016/S0960-9822(00)00401-2.
20. Yu, F., Morin, X., Cai, Y., Yang, X., and Chia, W. (2000). Analysis of partner of inscuteable, a novel player of Drosophila asymmetric divisions, reveals two distinct steps in inscuteable apical localization. Cell *100*, 399–409. https://doi.org/10.1016/s0092-8674(00)80676-5.
21. David, N.B., Martin, C.A., Segalen, M., Rosenfeld, F., Schweisguth, F., and Bellaïche, Y. (2005). Drosophila Ric-8 regulates Galphai cortical localization to promote Galphai-dependent planar orientation of the mitotic spindle during asymmetric cell division. Nat. Cell Biol. *7*, 1083–1090. https://doi.org/10.1038/ncb1319.

22. Chanet, S., Sharan, R., Khan, Z., and Martin, A.C. (2017). Myosin 2-induced mitotic rounding enables columnar epithelial cells to interpret cortical spindle positioning cues. Curr. Biol. *27*, 3350–3358.e3. https://doi.org/10.1016/j.cub.2017.09.039.

23. Niwayama, R., Moghe, P., Liu, Y.J., Fabrèges, D., Buchholz, F., Piel, M., and Hiiragi, T. (2019). A tug-of-war between cell shape and polarity controls division orientation to ensure robust patterning in the mouse blastocyst. Dev. Cell *51*, 564–574.e6. https://doi.org/10.1016/j.devcel.2019.10.012.

24. Godard, B.G., Dumollard, R., Heisenberg, C.P., and McDougall, A. (2021). Combined effect of cell geometry and polarity domains determines the orientation of unequal division. eLife *10*, e75639. https://doi.org/10.7554/eLife.75639.

25. Pierre, A., Sallé, J., Wühr, M., and Minc, N. (2016). Generic theoretical models to predict division patterns of cleaving embryos. Dev. Cell *39*, 667–682. https://doi.org/10.1016/j.devcel.2016.11.018.

26. Luxenburg, C., Pasolli, H.A., Williams, S.E., and Fuchs, E. (2011). Developmental roles for Srf, cortical cytoskeleton and cell shape in epidermal spindle orientation. Nat. Cell Biol. *13*, 203–214. https://doi.org/10.1038/ncb2163.

27. Lancaster, M.A., and Knoblich, J.A. (2012). Spindle orientation in mammalian cerebral cortical development. Curr. Opin. Neurobiol. *22*, 737–746. https://doi.org/10.1016/j.conb.2012.04.003.

28. Tan, D.W., and Barker, N. (2014). Intestinal stem cells and their defining niche. Curr. Top. Dev. Biol. *107*, 77–107. https://doi.org/10.1016/B978-0-12-416022-4.00003-2.

29. Gehart, H., and Clevers, H. (2019). Tales from the crypt: new insights into intestinal stem cells. Nat. Rev. Gastroenterol. Hepatol. *16*, 19–34. https://doi.org/10.1038/s41575-018-0081-y.

30. Fleming, E.S., Zajac, M., Moschenross, D.M., Montrose, D.C., Rosenberg, D.W., Cowan, A.E., and Tirnauer, J.S. (2007). Planar spindle orientation and asymmetric cytokinesis in the mouse small intestine. J. Histochem. Cytochem. *55*, 1173–1180. https://doi.org/10.1369/jhc.7A7234.2007.

31. Bellis, J., Duluc, I., Romagnolo, B., Perret, C., Faux, M.C., Dujardin, D., Formstone, C., Lightowler, S., Ramsay, R.G., Freund, J.N., and De Mey, J.R. (2012). The tumor suppressor Apc controls planar cell polarities central to gut homeostasis. J. Cell Biol. *198*, 331–341. https://doi.org/10.1083/jcb.201204086.

32. Spear, P.C., and Erickson, C.A. (2012). Apical movement during interkinetic nuclear migration is a two-step process. Dev. Biol. *370*, 33–41. https://doi.org/10.1016/j.ydbio.2012.06.031.

33. Carroll, T.D., Langlands, A.J., Osborne, J.M., Newton, I.P., Appleton, P.L., and Näthke, I. (2017). Interkinetic nuclear migration and basal tethering facilitates post-mitotic daughter separation in intestinal organoids. J. Cell Sci. *130*, 3862–3877. https://doi.org/10.1242/jcs.211656.

34. McKinley, K.L., Stuurman, N., Royer, L.A., Schartner, C., Castillo-Azofeifa, D., Delling, M., Klein, O.D., and Vale, R.D. (2018). Cellular aspect ratio and cell division mechanics underlie the patterning of cell progeny in diverse mammalian epithelia. eLife *7*, e36739. https://doi.org/10.7554/eLife.36739.

35. Fatehullah, A., Tan, S.H., and Barker, N. (2016). Organoids as an in vitro model of human development and disease. Nat. Cell Biol. *18*, 246–254. https://doi.org/10.1038/ncb3312.

36. Artegiani, B., and Clevers, H. (2018). Use and application of 3D-organoid technology. Hum. Mol. Genet. *27*, R99–R107. https://doi.org/10.1093/hmg/ddy187.

37. Schindelin, J., Arganda-Carreras, I., Frise, E., Kaynig, V., Longair, M., Pietzsch, T., Preibisch, S., Rueden, C., Saalfeld, S., Schmid, B., et al. (2012). Fiji: an open-source platform for biological-image analysis. Nat. Methods *9*, 676–682. https://doi.org/10.1038/nmeth.2019.

38. Meijering, E., Dzyubachyk, O., and Smal, I. (2012). Methods for cell and particle tracking. Methods Enzymol. *504*, 183–200. https://doi.org/10.1016/B978-0-12-391857-4.00009-4.

39. Bosveld, F., Markova, O., Guirao, B., Martin, C., Wang, Z., Pierre, A., Balakireva, M., Gaugue, I., Ainslie, A., Christophorou, N., et al. (2016). Epithelial tricellular junctions act as interphase cell shape sensors to orient mitosis. Nature *530*, 495–498. https://doi.org/10.1038/nature16970.

40. Minc, N., Burgess, D., and Chang, F. (2011). Influence of cell geometry on division-plane positioning. Cell *144*, 414–426. https://doi.org/10.1016/j.cell.2011.01.016.

41. Ershov, D., and Minc, N. (2019). Modeling embryonic cleavage patterns. Methods Mol. Biol. *1920*, 393–406. https://doi.org/10.1007/978-1-4939-9009-2_24.

42. Lechler, T., and Mapelli, M. (2021). Spindle positioning and its impact on vertebrate tissue architecture and cell fate. Nat. Rev. Mol. Cell Biol. *22*, 691–708. https://doi.org/10.1038/s41580-021-00384-4.

43. Sallé, J., and Minc, N. (2022). Cell division geometries as central organizers of early embryo development. Semin. Cell Dev. Biol. *130*, 3–11. https://doi.org/10.1016/j.semcdb.2021.08.004.

44. Nakajima, Y., Meyer, E.J., Kroesen, A., McKinney, S.A., and Gibson, M.C. (2013). Epithelial junctions maintain tissue architecture by directing planar spindle orientation. Nature *500*, 359–362. https://doi.org/10.1038/nature12335.

45. Théry, M., Racine, V., Pépin, A., Piel, M., Chen, Y., Sibarita, J.B., and Bornens, M. (2005). The extracellular matrix guides the orientation of the cell division axis. Nat. Cell Biol. *7*, 947–953. https://doi.org/10.1038/ncb1307.

46. Zheng, Z., Zhu, H., Wan, Q., Liu, J., Xiao, Z., Siderovski, D.P., and Du, Q. (2010). LGN regulates mitotic spindle orientation during epithelial morphogenesis. J. Cell Biol. *189*, 275–288. https://doi.org/10.1083/jcb.200910021.

47. Kotak, S., Busso, C., and Gönczy, P. (2012). Cortical dynein is critical for proper spindle positioning in human cells. J. Cell Biol. *199*, 97–110. https://doi.org/10.1083/jcb.201203166.

48. Wee, B., Johnston, C.A., Prehoda, K.E., and Doe, C.Q. (2011). Canoe binds RanGTP to promote Pins(TPR)/Mud-mediated spindle orientation. J. Cell Biol. *195*, 369–376. https://doi.org/10.1083/jcb.201102130.

49. Carminati, M., Gallini, S., Pirovano, L., Alfieri, A., Bisi, S., and Mapelli, M. (2016). Concomitant binding of Afadin to LGN and F-actin directs planar spindle orientation. Nat. Struct. Mol. Biol. *23*, 155–163. https://doi.org/10.1038/nsmb.3152.

50. Van Ness, J., and Pettijohn, D.E. (1983). Specific attachment of nuclear-mitotic apparatus protein to metaphase chromosomes and mitotic spindle poles: possible function in nuclear reassembly. J. Mol. Biol. *171*, 175–205. https://doi.org/10.1016/s0022-2836(83)80352-0.

51. Compton, D.A., and Cleveland, D.W. (1993). NuMA is required for the proper completion of mitosis. J. Cell Biol. *120*, 947–957.

52. Gloerich, M., Bianchini, J.M., Siemers, K.A., Cohen, D.J., and Nelson, W.J. (2017). Cell division orientation is coupled to cell-cell adhesion by the E-cadherin/LGN complex. Nat. Commun. *8*, 13996. https://doi.org/10.1038/ncomms13996.

53. Hart, K.C., Tan, J., Siemers, K.A., Sim, J.Y., Pruitt, B.L., Nelson, W.J., and Gloerich, M. (2017). E-cadherin and LGN align epithelial cell divisions with tissue tension independently of cell shape. Proc. Natl. Acad. Sci. USA *114*, E5845–E5853. https://doi.org/10.1073/pnas.1701703114.

54. Théry, M., Jiménez-Dalmaroni, A., Racine, V., Bornens, M., and Jülicher, F. (2007). Experimental and theoretical study of mitotic spindle orientation. Nature *447*, 493–496. https://doi.org/10.1038/nature05786.

55. Verde, F., Dogterom, M., Stelzer, E., Karsenti, E., and Leibler, S. (1992). Control of microtubule dynamics and length by cyclin A- and cyclin B-dependent kinases in Xenopus egg extracts. J. Cell Biol. *118*, 1097–1108. https://doi.org/10.1083/jcb.118.5.1097.

56. Stout, J.R., Yount, A.L., Powers, J.A., Leblanc, C., Ems-McClung, S.C., and Walczak, C.E. (2011). Kif18B interacts with EB1 and controls astral microtubule length during mitosis. Mol. Biol. Cell *22*, 3070–3080. https://doi.org/10.1091/mbc.E11-04-0363.

57. Grill, S.W., and Hyman, A.A. (2005). Spindle positioning by cortical pulling forces. Dev. Cell *8*, 461–465. https://doi.org/10.1016/j.devcel.2005.03.014.

58. Farhadifar, R., Yu, C.H., Fabig, G., Wu, H.Y., Stein, D.B., Rockman, M., Müller-Reichert, T., Shelley, M.J., and Needleman, D.J. (2020). Stoichiometric interactions explain spindle dynamics and scaling across 100 million years of nematode evolution. eLife *9*, e55877. https://doi.org/10.7554/eLife.55877.

59. McHugh, T., Gluszek, A.A., and Welburn, J.P.I. (2018). Microtubule end tethering of a processive kinesin-8 motor Kif18b is required for spindle positioning. J. Cell Biol. *217*, 2403–2416. https://doi.org/10.1083/jcb.201705209.

60. Moreci, R.S., and Lechler, T. (2021). KIF18B is a cell type-specific regulator of spindle orientation in the epidermis. Mol. Biol. Cell *32*, ar29. https://doi.org/10.1091/mbc.E21-06-0291.

61. Farin, H.F., Van Es, J.H., and Clevers, H. (2012). Redundant sources of Wnt regulate intestinal stem cells and promote formation of Paneth cells. Gastroenterology *143*, 1518–1529.e7. https://doi.org/10.1053/j.gastro.2012.08.031.

62. Sato, T., van Es, J.H., Snippert, H.J., Stange, D.E., Vries, R.G., van den Born, M., Barker, N., Shroyer, N.F., van de Wetering, M., and Clevers, H. (2011). Paneth cells constitute the niche for Lgr5 stem cells in intestinal crypts. Nature *469*, 415–418. https://doi.org/10.1038/nature09637.

63. Caussinus, E., and Gonzalez, C. (2005). Induction of tumor growth by altered stem-cell asymmetric division in Drosophila melanogaster. Nat. Genet. *37*, 1125–1129. https://doi.org/10.1038/ng1632.

64. Seldin, L., and Macara, I. (2017). Epithelial spindle orientation diversities and uncertainties: recent developments and lingering questions. F1000Res *6*, 984. https://doi.org/10.12688/f1000research.11370.1.

65. Wühr, M., Chen, Y., Dumont, S., Groen, A.C., Needleman, D.J., Salic, A., and Mitchison, T.J. (2008). Evidence for an upper limit to mitotic spindle length. Curr. Biol. *18*, 1256–1261. https://doi.org/10.1016/j.cub.2008.07.092.

66. Dimitracopoulos, A., Srivastava, P., Chaigne, A., Win, Z., Shlomovitz, R., Lancaster, O.M., Le Berre, M., Piel, M., Franze, K., Salbreux, G., et al. (2020). Mechanochemical crosstalk produces cell-intrinsic patterning of the cortex to orient the mitotic spindle. Curr. Biol. *30*, 3687–3696.e4. https://doi.org/10.1016/j.cub.2020.06.098.

67. Kiyomitsu, T., and Cheeseman, I.M. (2012). Chromosome- and spindle-pole-derived signals generate an intrinsic code for spindle position and orientation. Nat. Cell Biol. *14*, 311–317. https://doi.org/10.1038/ncb2440.

68. Scarpa, E., Finet, C., Blanchard, G.B., and Sanson, B. (2018). Actomyosin-driven tension at compartmental boundaries orients cell division independently of cell geometry *in vivo*. Dev. Cell *47*, 727–740.e6. https://doi.org/10.1016/j.devcel.2018.10.029.

69. Kelkar, M., Bohec, P., and Charras, G. (2020). Mechanics of the cellular actin cortex: from signalling to shape change. Curr. Opin. Cell Biol. *66*, 69–78. https://doi.org/10.1016/j.ceb.2020.05.008.

70. Schenk, J., Wilsch-Bräuninger, M., Calegari, F., and Huttner, W.B. (2009). Myosin II is required for interkinetic nuclear migration of neural progenitors. Proc. Natl. Acad. Sci. USA *106*, 16487–16492. https://doi.org/10.1073/pnas.0908928106.

71. Norden, C., Young, S., Link, B.A., and Harris, W.A. (2009). Actomyosin is the main driver of interkinetic nuclear migration in the retina. Cell *138*, 1195–1208. https://doi.org/10.1016/j.cell.2009.06.032.

72. Higashi, T., and Miller, A.L. (2017). Tricellular junctions: how to build junctions at the TRICkiest points of epithelial cells. Mol. Biol. Cell *28*, 2023–2034. https://doi.org/10.1091/mbc.E16-10-0697.

73. Bosveld, F., Wang, Z., and Bellaïche, Y. (2018). Tricellular junctions: a hot corner of epithelial biology. Curr. Opin. Cell Biol. *54*, 80–88. https://doi.org/10.1016/j.ceb.2018.05.002.

74. Mitchison, T.J., Ishihara, K., Nguyen, P., and Wühr, M. (2015). Size scaling of microtubule assemblies in early Xenopus Embryos. Cold Spring Harb. Perspect. Biol. *7*, a019182. https://doi.org/10.1101/cshperspect.a019182.

75. Lancaster, O.M., Le Berre, M., Dimitracopoulos, A., Bonazzi, D., Zlotek-Zlotkiewicz, E., Picone, R., Duke, T., Piel, M., and Baum, B. (2013). Mitotic rounding alters cell geometry to ensure efficient bipolar spindle formation. Dev. Cell *25*, 270–283. https://doi.org/10.1016/j.devcel.2013.03.014.

76. Zhu, J., Burakov, A., Rodionov, V., and Mogilner, A. (2010). Finding the cell center by a balance of dynein and myosin pulling and microtubule pushing: a computational study. Mol. Biol. Cell *21*, 4418–4427. https://doi.org/10.1091/mbc.E10-07-0627.

77. Jimenez, A.J., Schaeffer, A., De Pascalis, C., Letort, G., Vianay, B., Bornens, M., Piel, M., Blanchoin, L., and Théry, M. (2021). Acto-myosin network geometry defines centrosome position. Curr. Biol. *31*, 1206–1220.e5. https://doi.org/10.1016/j.cub.2021.01.002.

78. Hertwig, O. (1884). Das Problem der Befruchtung und der Isotropie des Eies, eine Theory der Vererbung. Jenaische Z. Naturwiss. *18*, 21–23.

79. Lechler, T., and Fuchs, E. (2005). Asymmetric cell divisions promote stratification and differentiation of mammalian skin. Nature *437*, 275–280. https://doi.org/10.1038/nature03922.

80. Biggs, L.C., Kim, C.S., Miroshnikova, Y.A., and Wickström, S.A. (2020). Mechanical forces in the skin: roles in tissue architecture, stability, and function. J. Invest. Dermatol. *140*, 284–290. https://doi.org/10.1016/j.jid.2019.06.137.

81. Luessing, J., Sakhteh, M., Sarai, N., Frizzell, L., Tsanov, N., Ramberg, K.O., Maretto, S., Crowley, P.B., and Lowndes, N.F. (2021). The nuclear kinesin KIF18B promotes 53BP1-mediated DNA double-strand break repair. Cell Rep. *35*, 109306. https://doi.org/10.1016/j.celrep.2021.109306.

82. Lough, K.J., Byrd, K.M., Descovich, C.P., Spitzer, D.C., Bergman, A.J., Beaudoin, G.M., 3rd, Reichardt, L.F., and Williams, S.E. (2019). Telophase correction refines division orientation in stratified epithelia. eLife *8*, e49249. https://doi.org/10.7554/eLife.49249.

83. Feng, Y., Sentani, K., Wiese, A., Sands, E., Green, M., Bommer, G.T., Cho, K.R., and Fearon, E.R. (2013). Sox9 induction, ectopic Paneth cells, and mitotic spindle axis defects in mouse colon adenomatous epithelium arising from conditional biallelic Apc inactivation. Am. J. Pathol. *183*, 493–503. https://doi.org/10.1016/j.ajpath.2013.04.013.

84. Dow, L.E., O'Rourke, K.P., Simon, J., Tschaharganeh, D.F., van Es, J.H., Clevers, H., and Lowe, S.W. (2015). Apc restoration promotes cellular differentiation and reestablishes crypt homeostasis in colorectal cancer. Cell *161*, 1539–1552. https://doi.org/10.1016/j.cell.2015.05.033.

85. Van Lidth de Jeude, J.F., Vermeulen, J.L., Montenegro-Miranda, P.S., Van den Brink, G.R., and Heijmans, J. (2015). A protocol for lentiviral transduction and downstream analysis of intestinal organoids. J. Vis. Exp. https://doi.org/10.3791/52531.

86. Krndija, D., El Marjou, F., Guirao, B., Richon, S., Leroy, O., Bellaiche, Y., Hannezo, E., and Matic Vignjevic, D. (2019). Active cell migration is critical for steady-state epithelial turnover in the gut. Science *365*, 705–710. https://doi.org/10.1126/science.aau3429.

87. Zhang, Y., Conti, M.A., Malide, D., Dong, F., Wang, A., Shmist, Y.A., Liu, C., Zerfas, P., Daniels, M.P., Chan, C.C., et al. (2012). Mouse models of MYH9-related disease: mutations in nonmuscle myosin II-A. Blood *119*, 238–250. https://doi.org/10.1182/blood-2011-06-358853.

88. Jacobelli, J., Friedman, R.S., Conti, M.A., Lennon-Dumenil, A.M., Piel, M., Sorensen, C.M., Adelstein, R.S., and Krummel, M.F. (2010). Confinement-optimized three-dimensional T cell amoeboid motility is modulated via myosin IIA-regulated adhesions. Nat. Immunol. *11*, 953–961. https://doi.org/10.1038/ni.1936.

89. Muzumdar, M.D., Tasic, B., Miyamichi, K., Li, L., and Luo, L. (2007). A global double-fluorescent Cre reporter mouse. Genesis *45*, 593–605. https://doi.org/10.1002/dvg.20335.

90. Sato, T., Stange, D.E., Ferrante, M., Vries, R.G., Van Es, J.H., Van den Brink, S., Van Houdt, W.J., Pronk, A., Van Gorp, J., Siersema, P.D., and

Clevers, H. (2011). Long-term expansion of epithelial organoids from human colon, adenoma, adenocarcinoma, and Barrett's epithelium. Gastroenterology *141*, 1762–1772. https://doi.org/10.1053/j.gastro.2011.07.050.

91. Goldspink, D.A., Matthews, Z.J., Lund, E.K., Wileman, T., and Mogensen, M.M. (2017). Immuno-fluorescent labeling of microtubules and centrosomal proteins in ex vivo intestinal tissue and 3D in vitro intestinal organoids. J. Vis. Exp. https://doi.org/10.3791/56662.

92. Salomon, J., Gaston, C., Magescas, J., Duvauchelle, B., Canioni, D., Sengmanivong, L., Mayeux, A., Michaux, G., Campeotto, F., Lemale, J., et al. (2017). Contractile forces at tricellular contacts modulate epithelial organization and monolayer integrity. Nat. Commun. *8*, 13998. https://doi.org/10.1038/ncomms13998.

93. Hara, Y., and Kimura, A. (2009). Cell-size-dependent spindle elongation in the Caenorhabditis elegans early embryo. Curr. Biol. *19*, 1549–1554. https://doi.org/10.1016/j.cub.2009.07.050.

94. Wadell, H. (1935). Volume, shape, and roundness of quartz particles. J. Geol. *43*, 250–280.

95. Gambarotto, D., Zwettler, F.U., Le Guennec, M., Schmidt-Cernohorska, M., Fortun, D., Borgers, S., Heine, J., Schloetel, J.G., Reuss, M., Unser, M., et al. (2019). Imaging cellular ultrastructures using expansion microscopy (U-ExM). Nat. Methods *16*, 71–74. https://doi.org/10.1038/s41592-018-0238-1.

STAR★METHODS

KEY RESOURCES TABLE

REAGENT or RESOURCE	SOURCE	IDENTIFIER
Antibodies		
Mouse monoclonal anti-α-tubulin (clone DM1A)	Sigma-Aldrich	Cat#T9026; RRID:AB_2617116
Rabbit polyclonal anti-EpCAM	Abcam	Cat#ab71916; RRID:AB_1603782
Rabbit polyclonal anti-afadin	Abcam	Cat#ab11337; RRID:AB_297943
Rabbit polyclonal anti-alpha-tubulin	Abcam	Cat#ab18251; RRID:AB_2210057
Mouse monoclonal anti-E-cadherin (clone 36)	BD Biosciences	Cat#610181; RRID:AB_397580
Rabbit polyclonal anti-Phospho-MyosinLightChain2	Cell Signaling	Cat#3671; RRID:AB_330248
Rabbit monoclonal anti-E-cadherin (clone 24E10)	Cell Signaling	Cat#3195S; RRID:AB_2291471
Mouse monoclonal anti-dynein	Millipore	Cat#MAB1618; RRID:AB_2246059
Rabbit monoclonal anti-NuMA	Abcam	Cat#ab109262; RRID:AB_10863599
Rabbit polyclonal anti-non-muscle Myosin Heavy chain II-A (clone poly19098)	Biolegend	Cat#909801; RRID:AB_2565100
Mouse monoclonal anti-GAPDH	Proteintech	Cat#60004-1-Ig; RRID:AB_2107436
Rabbit polyclonal anti-Kif18B	ThermoFisher Scientific	Cat#A303-982A-T; RRID:AB_2620331
Rabbit polyclonal anti-Kif18B	Biorbyt	Cat#orb612187
Goat anti-mouse-Alexa488	Life Technologies	Cat#A11001; RRID:AB_2534069
Goat anti-mouse-Alexa568	Life Technologies	Cat#A11004; RRID:AB_2534072
Goat anti-rabbit-Alexa488	Life Technologies	Cat#A11008; RRID:AB_143165
Goat anti-rabbit-Alexa568	Life Technologies	Cat#A11011; RRID:AB_143157
Goat anti-rabbit-Alexa647	Life Technologies	Cat#A21446: RRID:AB_10371940
HRP-linked goat anti-mouse IgG antibody	Sigma-Aldrich	Cat#A9044; RRID:AB_258431
HRP-linked donkey anti-rabbit IgG antibody	Invitrogen	Cat#31460; RRID:AB_228341
Bacterial and virus strains		
Lentiviral biosensors LentiBrite α-tubulin-GFP	Merck	Cat#17-10206
Lentiviral biosensors LentiBrite EB3-RFP	Merck	Cat#17-10222
Edit-R All-in-one lentiviral system, set of 3 lentiviral sgRNAs to target Kif18B	Horizon Discovery	Cat#GSGM11839-246783580, #GSGM11839-246783577, #GSGM11839-246783579
Edit-R All-in-one lentiviral system, non-targeting sgRNA	Horizon Discovery	Cat#GSG11811
Biological samples		
Human colon organoids COL-2920xi	Audrey Vincent (CANTHER, Lille)	ORGALille Core Facility
Chemicals, peptides, and recombinant proteins		
DMEM/F12	Thermo Fisher Scientific	Cat#12634010
Matrigel	VWR	Cat#734-1100
IntestiCult™ Organoid Growth medium	STEMCELL Technologies	Cat#06005
TrypLE Express	Thermo Fisher Scientific	Cat#12605010
CHIR99021	STEMCELL Technologies	Cat#72054
Y-27632	STEMCELL Technologies	Cat#72304
4-hydroxytamoxifen	Sigma-Aldrich	Cat#SML1666
Puromycin	Thermo Fisher Scientific	Cat#A1113803

(Continued on next page)

Continued

REAGENT or RESOURCE	SOURCE	IDENTIFIER
Doxycycline	Merck	Cat#D9891
EGF	Peprotech	Cat#236-EG
B-27® Supplement Minus Vitamin A	Thermo Fisher Scientific	Cat#12587010
N-2 Supplement	Thermo Fisher Scientific	Cat#17502048
A83-01	Tocris	Cat#2939
Gastrin	Sigma-Aldrich	Cat#G9020
Y-27632	Tocris	Cat#1254
Hoechst 33342	Life Technologies	Cat#H3570
Blebbistatin	Sigma-Aldrich	Cat#B0560
Nocodazole	Sigma-Aldrich	Cat#M1404
Spy650-Tubulin	Spirochrome, Cytoskeleton	Cat#CY-SC503
Gentle Cell Dissociation Reagent	STEMCELL Technologies	Cat#07174
Goat serum	Sigma-Aldrich	Cat#G9023
Vectashield	Vectashield, Eurobio	Cat#H-1000
Experimental models: Cell lines and organoid lines		
L-WNR cell line	ATCC	Cat# CRL-3276; RRID:CVL_DA06
α-tubulin-GFP/H2B-mCherry organoids	This manuscript	N/A
VillinCreERT2-tdTomato organoids	This manuscript	N/A
Myosin-IIA-GFP-knock-in organoids	This manuscript	N/A
Myosin-IIA-KO/mTmG organoids	This manuscript	N/A
Control-KO organoids	This manuscript	N/A
Kif18B-KO organoids	This manuscript	N/A
EB3-RFP organoids	This manuscript	N/A
Experimental models: Organisms/strains		
Wild-type C57/Bl6 mice	Institut Jacques Monod animal house facility, Paris	N/A
H2B-mCherry-knock-in C57/Bl6 mice	Renata Basto (Institut Curie, Paris)	N/A
VillinCreERT2-tdTomato C57/Bl6 mice	Danijela Vignjevic (Institut Curie, Paris)	N/A
Myosin-IIA-GFP-knock-in C57/Bl6 mice	Robert Adelstein (National Heart Lung and Blood Institute, Bethesda), Ana-Maria Lennon-Dumesnil (Institut Curie, Paris)	N/A
Myosin-IIA-KO/mTmG C57/Bl6 mice	Danijela Vignjevic (Institut Curie, Paris)	N/A
Software and algorithms		
FiJi	Schindelin et al.[37]	https://fiji.sc/; RRID:SCR_002285
Metamorph	Molecular Devices	https://www.moleculardevices.com/products/cellular-imaging-systems/acquisition-and-analysis-software/metamorph-microscopy; RRID:SCR_002368
ImageJ plugin MTrack J	Meijering et al.[38]	https://imagescience.org/meijering/software/mtrackj/
Matlab	MathWorks	mathworks.com/products/matlab.html; RRID:SCR_001622
Meshlab	Visual Computing Lab	www.meshlab.net
Prism 9	GraphPad	www.graphpad.com/features; RRID:SCR_002798
2D models for spindle orientation	Bosveld et al.[39] and Minc et al.[40]	N/A
3D models for spindle orientation	Ershov and Minc[41] and Pierre et al.[25]	N/A
GenerateMesh.py code	This paper	https://zenodo.org/badge/latestdoi/623985418

(*Continued on next page*)

Continued

REAGENT or RESOURCE	SOURCE	IDENTIFIER
GetJunctions.py code	This paper	https://zenodo.org/badge/latestdoi/623985418
Deposited data		
Source data files for quantification	Zenoda	https://doi.org/10.5281/zenodo.7804776

RESOURCE AVAILABILITY

Lead contact

Further information and requests for resources and reagents should be directed and will be fulfilled by the lead contacts, Delphine Delacour (delphine.delacour@univ-amu.fr).

Materials availability

Materials generated in the current study are available from the lead contact upon request. There are restrictions to the availability of materials due to collaborations or MTAs.

Data and code availability

Source data files have been deposited at Zenodo (https://doi.org/10.5281/zenodo.7804776). Microscopy data reported in this paper will be shared by the lead contact on request. Original codes for segmentation prior to MeshLab 3D viewing and cell contact mapping have been deposited at Zenodo (https://doi.org/10.5281/zenodo.7802531). DOIs are listed in the key resources table. Any additional information required to reanalyze the data reported in this paper is available from the lead contact upon request.

EXPERIMENTAL MODEL AND SUBJECT DETAILS

Organoid cultures and transfection

Wild-type C57/Bl6 adult male mice were provided by the animal house facility of the Institut Jacques Monod. Mice were housed in EOPS (Environment without Specific Pathogenic Organisms) environment, and handled in accordance with French regulation for animal care. Experiments were performed with ethical approval of the Comité d'Ethique Buffon (Institut Jacques Monod). Mice used for intestinal crypt isolation were between 6 and 12 weeks old. After euthanization by cervical dislocation, the small intestine was harvested, flushed with PBS to discard luminal content and cut longitudinally open. The tissue was then cut into small pieces of 3-5 mm and further washed in PBS. The pieces of intestinal tissue were then incubated on ice for 10 min in a tube containing 5 mM EDTA. The tube was then vortexed for 2 min to release villi from the tissue. After EDTA removal, the intestinal pieces were placed in cold PBS and vortexed vigorously for 3 min to ensure crypt release. This process was repeated 3 times, with each fraction recovered. The third and fourth fractions are usually concentrated in crypts, so these were combined and passed through a 70-μm cell strainer to remove remaining villi and centrifuged at 1000 RPM for 5 min. The pellet (crypts) was then washed in advanced DMEM/F12 (#12634010 Thermo Fisher Scientific, Waltham, Massachusetts, USA) and centrifuged. The final pellet is resuspended in 50 μl of 1:1 ratio of advanced DMEM/F12 and ice-cold Matrigel (#734-1100 VWR, Radnor, PA, USA) and plated as domes. Incubation at 37°C for 20-30 min allowed Matrigel polymerization. Organoid culture was performed in IntestiCult™ Organoid Growth medium (#06005 STEMCELL Technologies, Vancouver, Canada), from here on termed ENR medium. Organoids were routinely grown in Matrigel with IntestiCult™ Organoid Growth medium and passaged every 7 to 10 days. Medium was changed every 2 days. Live-imaging or immunofluorescence experiments were performed on 3-4 days organoids. For cystic growth, intestinal organoids were cultured with L-WNR medium supplemented with 10μM CHIR99021 for 10 days. The L-WNR cell line was purchased from ATCC (ATCC CRL-3276™). The L-WNR medium was produced according to the ATCC recommendations.

α-tubulin-GFP and EB3-RFP expression was carried out by lentiviral transduction using the commercial lentiviral biosensors LentiBrite (#17-10206; #17-10222, Merck, Darmstadt, Germany) and following an already established protocol for lentiviral transduction in intestinal organoids[85]. This process involves dissociating intestinal organoids into single cells using TrypLE Express (#12605010 Thermo Fisher Scientific, Waltham, Massachusetts, USA) and seeding on a layer of Matrigel along the lentiviral vectors overnight, before covering with another layer of Matrigel the next day to allow growth into 3D organoids. The medium was enriched with 10 μM of CHIR99021 and 10 μM of Y-27632 (#72054 and #72304 STEMCELL Technologies, Vancouver, Canada) to prioritize stem cell proliferation and improve single cell survival respectively. After 48 to 72h, fluorescent organoids start appearing and can be isolated and expanded.

H2B-mCherry organoids were generated from H2B-mCherry-knock-in mice provided by Renata Basto (Institut Curie, Paris). VillinCreERT2-tdTomato organoids were generated from mice provided by Danijela Vignjevic (Insitut Curite, Paris)[86] Myosin-IIA-GFP-knock-in mice[87] were provided by Robert S. Adelstein (NHLBI, Bethesda) and Ana-Maria Lennon-Dumesnil (Institut Curie, Paris). Myosin-IIA-KO/mTmG mice[86] were kindly provided by Danijela Vignjevic (Insitut Curite, Paris) and generated by crossing

Myosin-IIA-KO[88] and mTmG mice[89]. Cre recombinase for Myosin-IIA-KO was induced with 100nM of 4-hydroxytamoxifen for 24h (#SML1666, Sigma-Aldrich).

Kif18B-KO organoids were generated by a CRISPR-Cas9 strategy using the Edit-R All-in-one lentiviral system from Horizon Discovery (Cambridge, UK). A set of 3 lentiviral sgRNAs were used to target Kif18B (#GSGM11839-246783580: GGTCAGAACAC CCAGTTAAT; #GSGM11839-246783577: GTGTTTGCCTATGGCGCCAC; #GSGM11839-246783579: GTGGTGTTGAGGTCCC GAGT). Control-KO organoids were generated using a non-targeting sgRNA (#GSG11811, Horizon Discovery). Organoids were transduced with lentiviral particles containing an inducible Cas9 along the sgRNAs for the targeted gene. Selection was then performed using 2ug/ml of puromycin (#A1113803, Thermo Fisher Scientific) for at least 2 weeks before inducing Cas9 with 600 ng/ml of doxycycline (#D9891 Merck).

For human organoid preparation, the project was approved by the Scientific Committee of the tumor bank of Lille and the Department of Pathology of the Lille University Hospital. The patient had signed an informed consent. Left colectomy was carried out for a colon adenocarcinoma in the Department of General and Digestive Surgery of the Lille University Hospital. The patient had not been treated with neoadjuvant chemotherapy. The normal mucosa sample (1 cm2 harvested >10cm distant from the tumor) was cut into small pieces (<3mm^3) and washed thoroughly with 1X PBS buffer supplemented with combined antibiotics (normocin, gentamicin and amphotericin B). Mucosa fragments were then incubated in 25 ml of 1X PBS with 2.5mM EDTA at 4°C for 30 min under slow rotation. Mechanical release of colonic crypts was then performed three times in 10 mL 1X PBS. Fractions of colonic crypt suspension were pooled, centrifuged, resuspended in advanced DMEM/F12 medium and filtered through a 70-μm cell strainer. After counting, cells were resuspended in Matrigel and seeded in 40 μl domes in the wells of a 24-well plate. After Matrigel solidification, domes were covered with complete colon organoid medium (advanced DMEM/F12 medium supplemented with 1X Glutamax (Invitrogen), 1 X HEPES (Sigma-Aldrich), B-27® Supplement Minus Vitamin A (Thermo Fisher Scientific), 1 X N2 (Thermo Fisher Scientific), 1 mM N-acetyl-L-cysteine (Sigma-Aldrich), 50% v/v Wnt3a/R-Spondin-1/Noggin-conditioned medium, 50 ng/ml EGF (Peprotech), 0.5 μM A83-01 (Tocris), 10 mM Nicotinamide (Sigma-Aldrich), 10 nM Gastrin (Sigma-Aldrich) and 10 μM Y-27632 dihydrochloride (Tocris), as recommended in Sato et al.[90]. Resulting colonic organoids were named COL-2920xi. Complete medium without Y-27632 was then renewed every two days and organoids were passaged through mechanical disruption every week.

METHOD DETAILS

Antibodies and reagents

Mouse monoclonal antibody directed against α-tubulin (clone DM1A, IF dilution, 1:100) was purchased from Sigma-Aldrich. Rabbit polyclonal antibody directed against EpCAM (#ab71916, IF dilution, 1:100), rabbit polyclonal against afadin (#ab11337, IF dilution 1:100), rabbit polyclonal antibody directed against α-tubulin (#ab18251, IF 1:100) were from Abcam. Mouse monoclonal antibody directed against E-cadherin (clone 36, #610181, IF dilution, 1:50) was from BD Biosciences. Rabbit polyclonal antibody directed against Phospho-Myosin Light Chain 2 (Ser19, #3671, IF dilution, 1:100) and rabbit monoclonal antibody directed against E-cadherin (clone 24E10, #3195S, IF dilution 1:100) were from Cell Signaling Technology. Mouse monoclonal antibody against dynein (#MAB1618, IF dilution 1:100) was from Millipore. Rabbit monoclonal antibody directed against NuMA (EP3976, #ab109262, IF dilution, 1:100) was from Abcam. Rabbit polyclonal antibody directed against non-muscle myosin heavy chain II-A antibody (clone poly19098, #909801, WB dilution 1:500) was from Biolegend. Mouse monoclonal antibody directed against GAPDH (#60004-1-Ig, WB dilution 1:5000) was from Proteintech. Rabbit polyclonal antibody against Kif18B (#A303-982A-T, WB dilution 1:500; #orb612187, IF dilution 1:100) were from ThermoFisher Scientific and Biorbyt, respectively. Goat anti-mouse-Alexa-488, 568, anti-rabbit-Alexa488, 568 or 647 were from Life Technologies (Paisley, UK). Nuclei were stained with Hoechst 33342 solution incubation (Life Technologies) at a 1:1000 dilution. Blebbistatin, Y-27632 and nocodazole were from Sigma Aldrich (Saint-Louis, MO, USA). Spy650-Tubulin was obtained from Cytoskeleton (Denver, USA).

Drug treatments

Organoids were incubated in 25μM blebbistatin or 150nM nocodazole for 1.5h, then washed out with PBS and prepared for immunostaining or live-imaging. Cells were incubated for 1.5h in DMSO as controls.

Biochemical analysis

For western blots, organoid lysates were prepared 3 days after plating using per condition 6 wells of a 24-well plate. Matrigel was depolymerized by incubating with 1 ml of Gentle Cell Dissociation Reagent (#07174 STEMCELL Technologies, Vancouver, Canada) for 30 min at 4°C and centrifugation for 5 min at 500 x g at 4°C. The pellet was resuspended in lysis buffer containing 25mM Tris / 5 mM NaCl / 1mM EDTA / 1mM EGTA / 0.5% NP40 / 1% Triton TX100, and incubated on ice for 30 min. The solution was then passed 10 times through a syringe equipped with a 23G needle and centrifuged at 10 000 RPM at 4°C for 10 min. Supernatant total protein content was measured by Bradford assay (Biorad). For each condition, 50μg of proteins was loaded per well in Novex Tris-Glycine precast gels (ThermoFischer Scientific). Proteins were detected with either HRP-linked goat anti-mouse IgG antibody (dilution 1:10,000; Sigma-Aldrich) or HRP-linked donkey anti-rabbit IgG antibody (dilution 1:10,000, Invitrogen), and visualized on ImageQuant LAS4000 (GE-Healthcare, Buckinghamshire, UK). Signal quantification was performed using Fiji software.

Immunostaining

Routinely, organoids were fixed using 4% paraformaldehyde for 30 min, then permeabilized using 0.025% saponin solution in PBS for 30 min. Blocking step was performed in 0.025% saponin/1% BSA solution for 45 min, before proceeding to incubation with primary antibody at 4°C overnight. The next day, the primary antibody was removed and the organoids washed 3 times in PBS for 10 min each, before adding the secondary antibody and left to incubate for 2h at room temperature. Finally, organoids were washed 3 times again for 10 min before incubating in Hoechst 33342 for 15 min to stain nuclei. Immunostained samples were mounted in home-made Mowiol solution.

For the MT immunostaining, we used an established protocol that maintain the MT integrity in intestinal organoids[91]. Briefly, organoids were isolated from the Matrigel and fixed in a methanol/formaldehyde solution (92% methanol, 8% formaldehyde). The blocking step was performed by incubating organoids in 10% goat serum solution in PBS with 0.1% Triton X-100. Immunostained organoids were mounted in home-made Mowiol solution on a slide.

For E-cadherin immunostaining *in vivo*, mouse jejunum was processed as previously described[92]. Briefly, samples were fixed for 2 h in 4% PFA and paraffin embedded. 5 μm tissue sections were de-waxed in a xylene bath, rehydrated in isopropanol and in solutions with decreasing ethanol concentrations. Tissue sections were then blocked in 10% goat serum (Sigma-Aldrich) for 1 h. Primary antibody incubation was performed at 4°C overnight and secondary antibody incubation at room temperature for 2 h, both in 1% goat serum solution. Hoechst33342 staining was used to detect nuclei. Tissue sections were mounted in home-made Mowiol 488 solution.

For NuMA immunostaining *in vivo*, 1-mm pieces of mouse jejunum were fixed in 4% PFA overnight under shaking. After PBS wash, tissue permeabilization was performed in 1% Triton X-100 / PBS solution for 1 h, before saturation in 1% BSA / 3% goat serum / 0.2% Triton X-100 / PBS solution for 1 h. Incubation with primary or secondary antibodies were done in 0.1% BSA / 0.3 % goat serum / 0.2 % Triton X-100 / PBS overnight at 4°C. Hoechst33342 staining was used to detect nuclei. Immunostained samples were mounted in Vectashield (Vector Laboratories, Burlingame, CA).

Live imaging

Dynamics experiments on α-tubulin-GFP/H2B-mCherry, myosin-IIA-KI-GFP, EB3-RFP or Spy650-Tubulin organoids were performed using an inverted Zeiss microscope equipped with a CSU-X1 spinning disk head (Yokogawa – Andor), using Zeiss 40X and 63X water objectives. Spindle pole oscillations during metaphase have been analyzed using the ImageJ plugin MTrack J [38].

Laser ablation experiments

Laser ablation experiments were performed using a spinning disk microscope equipped with a CSU-XI spinning disk head, using a 63X oil objective. The ablation was done using a pulsed 355 nm ultraviolet laser at a power of 30% and a thickness of 3, interfaced with an iLas system (Roper Scientific) piloted in Metamorph.

Two-dimensional models for spindle orientation

2D models to predict spindle orientation were adapted from Minc et al.[40] and Bosveld et al.[39]. These models were developed and executed through Matlab (Mathworks) scripts which can be made available upon demand. Starting from the shape of a cell, the model positioned spindle poles and traced MT asters radiating from spindle poles to the contour. For length limitations, we added a fixed maximal length to MTs, normalized to cell length along the A-B axis, which was varied in Figure 2E. Each MT is associated to a force, f_{MT}, which varies depending on hypothesis. For models based on shape sensing, we posited that $f_{MT} = aL_{MT}^2$ with L_{MT} the length of the MT and *a*, an arbitrary constant. The scaling to the square was chosen as it best represents a length-dependent system in which MTs pull at the surface[40,93]. We note however that other models previously proposed to center and orient spindles with the long axis, including those based on pulling in bulk cytoplasm or MT pushing at the surface and limited by buckling, yielded to the same outputs. For NuMA based models, the force per MT was $f_{MT} = b[NuMA]^*L_{MT}^2$, with b an arbitrary constant, and [NuMA] is the local concentration of NuMA around cells, inputted as a normalized Gaussian distribution with a peak located at the basal pole of cells. The script then looped to compute the torque exert generated by all MTs as a function of all possible spindle angles, and computed a rotational energy potential as a primitive of the torque[54] (Figure 2F). Free parameters in the model were the number of MTs, the size of the spindle and the spatial extension of asters, which had little influence on model prediction (Figures S3A–S3D). For the NuMA model, we added one other parameter which is the width of the Gaussian, which was estimated from experimental images, and which did not influence prediction for domain size relatively small as compared to cell contour. Key parameters that altered spindle orientation outputs were thus cell shape, and the asymmetry of spindle positioning, as well as the maximal length of MTs related to cell length (Figures 2G, 2H, and S3A–S3D)

Three-dimensional simulations for spindle position and orientation

The simulation package used for 3D models was developed in Matlab and was adapted from Pierre et al.[25] and Ershov et al.[41]. This package includes a module to extract and reconstitute 3D shapes, spindle pole positions and polarity domains from segmented experimental image, and to add predefined hypothesis similar to those used above in 2D. In 3D, the exclusion of MTs from the basal pole was introduced as a gradient from the basal pole of length limitation, which was scaled to cell length along the A-B axis. The size of spindles and polar basal domains were defined directly from each experimental stack. Once parameters were defined as inputs, the model placed the spindle in a random position and orientation, traced MTs from spindle poles to measure their length and

Please cite this article in press as: Saleh et al., Length limitation of astral microtubules orients cell divisions in murine intestinal crypts, Developmental Cell (2023), https://doi.org/10.1016/j.devcel.2023.06.004

associated a force to each, and computed both global forces and torques exerted by MT asters. To search for minima, the model used a random walk, which follows the minimization of torques and forces. This was achieved by randomly modulating one of the 5 spatial parameters (3 for the position and 2 for the orientation of spindles), and recalculating the force torque at the subsequent step. The simulations followed the direction of force/torque minimization and stopped at a position/orientation once the iteration returns to this equilibrium after a given number of iterations (e.g. 300 runs) (Figures 4E–4G and S5A–S5C; Videos S4 and S5). The length of the simulations, the duration needed to identify a stable equilibrium, the noise added to explore other parameters, and other intrinsic parameters of the loop, can be modulated, but were fixed for all the simulations performed in this work. Finally, to ensure that the spindle position/orientation identified did not correspond to a local minimum which could have been biased by the initial conditions, the simulations were run typically 3-4 times from another random starting position/orientation. Finally, once a position was found, the model recalculated the torque landscapes as a function of the 2 possible angles (Figure S5C).

Segmentation and 3D rendering

Cell shape or spindle pole 3D segmentations are performed based on confocal z-stacks of cell membranes (i.e. E-cadherin, EpCAM) or MTs (i.e. α-tubulin, NuMA), respectively. Segmentations are performed manually to guarantee the best match with the initial data. Masks corresponding to cell shapes, spindle poles, organoid lumen and basal environment (“exterior”) were generated on each slice of confocal z-stacks using Fiji [37].

For generating the 3D rendering of organoid cells, mask outlines were translated into meshes, which are 3D surfaces connecting the perimeters on each slice, by using a Python program adapted from an initial program provided by Emmanuel Faure (LIRMM, Montpellier). Briefly, for a given cell, the mask was first translated into a list of points lying on the perimeters for every position along z where the cell is present. The list of points was then translated into a list of polygonal faces linking the points together. Visualization of meshes was done with the Meshlab software (www.meshlab.net).

Measurements of geometric properties of the segmented cells, in particular their volume V and surface area A, were provided by Meshlab and used to compute the cell sphericity: s=π1/3(6V)2/3/A[94]. From each pixel of the segmented cells, we computed the distance to the lumen. For each cell, the mean cell height H in the apico-basal direction was computed as the difference between the furthest and closest pixels from the lumen, averaged for every position along z where the cell is present. The mean cell width was computed from the cell volume and height assuming a cylindrical geometry and using W=2(V/πH)½. The mean spindle positioning with respect to the apico-basal axis was computed by averaging the distance from each point of the spindle to the lumen.

Multicellular contact distribution was computed from the ImageJ organoid cell shape masks and by using a custom Python program. The multicellular contacts were identified as any pixel in the vicinity of the borders of three or more cell masks (within 20 pixels). The “degree” of the multicellular contact (3-cells, 4-cells etc.) was given by the number of different cell masks in the vicinity of each multicellular contact. Positioning of computed multicellular contacts was then visualized together with cell meshes in Meshlab.

Expansion microscopy of organoids

Expansion microscopy protocol was adapted from Gambarotto et al.[95]. Matrigel domes containing mouse organoids were dissociated by using Gentle Cell Dissociation Reagent. After centrifugation, Matrigel debris were eliminated with the supernatant and organoid pellet kept. Organoids were incubated overnight at 37°C in PBS containing 2% acrylamide / 1.5% formaldehyde.

For gelation, organoids were washed in PBS and pelleted by centrifugation. After resuspension PBS, organoids were layed on a parafilm piece in a humid chamber. After PBS removal with a tip, gelation solution (19.3% sodium acrylate / 10% acrylamide / 0.1% N,N’-methylenbisacrylamide / 0.5% TEMED / 0.1% ammonium persulfate, in PBS) was added. Gelation solution containing organoids was covered with a 5mm coverslip, incubated 5 min on ice and then 1 h at 37°C. The coverslip and the gel were placed in a 24-well plate filled with 500µl of denaturation buffer (200mM SDS / 200mM NaCl / 50mM Tris water, PH9). After 15 min agitation at room temperature, the gel detached from the coverslip, was placed in a 1.5ml microtube filled with denaturation buffer and incubated at 95°C for 1h30min.

For immunofluorescence, organoids were transferred in a 24-well plate, blocked and permeabilized during incubation in 1% BSA / 0.025% saponin, in PBS solution for 1 h at room temperature. Primary antibodies were incubated overnight at 4°C in the 1% BSA / 0.025% saponin, in PBS solution, under gentle shacking. The day after, after 3 PBS washes, secondary antibodies were incubated 4 h at 4°C and then 1 h at room temperature upon gentle shacking. After three PBS washes, nuclei were labelled with Hoechst 33342.

For the organoid expansion, the gel was transferred in a 6-well plate filled with ddH2O and wash for 1 h without agitation. After ddH2O change, the gel was incubated overnight at room temperature. The day after, the expansion index was evaluated based on gel length before and after expansion. For image acquisition, the expanded gel was placed in a poly L-lysine-coated glass chamber after exceeding water removal.

QUANTIFICATION AND STATISTICAL ANALYSIS

All statistical analyses were performed using Prism (GraphPad Software, San Diego, CA, USA, version 9.0). Statistical details of experiments can be found in the figure legends. Unless otherwise stated, experiments were replicated 3 times independently. No sample size estimations and no blinding were performed.